



Scintillation light detection in the 6-m drift-length ProtoDUNE Dual Phase liquid argon TPC

DUNE Collaboration

A. Abed Abud^{36,127}, B. Abi¹⁵⁴, R. Acciarri⁶⁷, M. A. Acero¹¹, M. R. Adames¹⁹⁰, G. Adamov⁷², M. Adamowski⁶⁷, D. Adams²¹, M. Adinolfi²⁰, A. Aduszkiewicz⁸¹, J. Aguilar¹²⁵, Z. Ahmad²⁰¹, J. Ahmed²⁰⁴, B. Aimard⁵³, B. Ali-Mohammadzadeh^{32,93}, T. Alion¹⁸⁸, K. Allison⁴⁴, S. Alonso Monsalve^{36,60}, M. AlRashed¹¹⁷, C. Alt⁶⁰, A. Alton¹², R. Alvarez⁴⁰, P. Amedo⁸⁶, J. Anderson⁷, C. Andreopoulos^{127,175}, M. Andreotti^{68,94}, M. Andrews⁶⁷, F. Andrianala⁵, S. Andringa¹²⁶, N. Anfimov¹¹⁵, A. Ankowski¹⁸⁰, M. Antoniassi¹⁹⁰, M. Antonova⁸⁵, A. Antoshkin¹¹⁵, S. Antusch¹⁴, A. Aranda-Fernandez⁴³, L. Arellano¹³³, L. O. Arnold⁴⁶, M. A. Arroyave⁵⁹, J. Asaadi¹⁹³, L. Asquith¹⁸⁸, A. Aurisano⁴¹, V. Aushev¹²³, D. Autiero¹⁰⁸, V. Ayala Lara¹⁰³, M. Ayala-Torres⁴², F. Azfar¹⁵⁴, A. Back⁹¹, H. Back¹⁵⁵, J. J. Back²⁰⁴, C. Backhouse¹⁹⁹, I. Bagaturia⁷², L. Bagby⁶⁷, N. Balashov¹¹⁵, S. Balasubramanian⁶⁷, P. Baldi²⁵, B. Baller⁶⁷, B. Bambah⁸², F. Barao^{110,126}, G. Barenboim⁸⁵, P. Barham Alzas³⁶, G. Barker²⁰⁴, W. Barkhouse¹⁴⁷, C. Barnes¹³⁷, G. Barr¹⁵⁴, J. Barranco Monarca⁷⁷, A. Barros¹⁹⁰, N. Barros^{61,126}, J. L. Barrow¹³⁴, A. Basharina-Freshville¹⁹⁹, A. Bashyal⁷, V. Basque¹³³, C. Batchelor⁵⁸, E. Batista das Chagas³¹, J. B. R. Battat²⁰⁵, F. Battisti¹⁵⁴, F. Bay⁴, M. C. Q. Bazetto³¹, J. L. L. Bazo Alba¹⁶⁷, J. F. Beacom¹⁵², E. Bechetoille¹⁰⁸, B. Behera⁴⁵, C. Beigbeder¹⁵⁸, L. Bellantoni⁶⁷, G. Bellettini¹⁶⁵, V. Bellini^{32,93}, O. Beltramello³⁶, N. Benekos³⁶, C. Benitez Montiel⁹, F. Bento Neves¹²⁶, J. Berger⁴⁵, S. Berkman⁶⁷, P. Bernardini^{96,176}, R. M. Berner¹⁵, A. Bersani⁹⁵, S. Bertolucci^{18,92}, M. Betancourt⁶⁷, A. Betancur Rodriguez⁵⁹, A. Bevan¹⁷⁰, Y. Bezawada²⁴, T. J. C. Bezerra¹⁸⁸, A. Bhardwaj¹²⁹, V. Bhatnagar¹⁵⁷, M. Bhattacharjee⁸⁹, D. Bhattarai¹⁴³, S. Bhuller²⁰, B. Bhuyan⁸⁹, S. Biagi¹⁰², J. Bian²⁵, M. Biassoni⁹⁷, K. Biery⁶⁷, B. Bilki^{16,106}, M. Bishai²¹, A. Bitadze¹³³, A. Blake¹²⁴, F. Blaszczyk⁶⁷, G. C. Blazey¹⁴⁸, E. Blucher³⁸, J. Boissevain¹²⁸, S. Bolognesi³⁵, T. Bolton¹¹⁷, L. Bomben^{97,105}, M. Bonesini^{97,139}, M. Bongrand¹⁵⁸, C. Bonilla-Diaz³³, F. Bonini²¹, A. Booth¹⁷⁰, F. Boran¹⁶, S. Bordini³⁶, A. Borkum¹⁸⁸, N. Bostan¹⁵⁰, P. Bour⁵⁰, C. Bourgeois¹⁵⁸, D. Boyden¹⁴⁸, J. Bracinek¹⁷, D. Braga⁶⁷, D. Brailsford¹²⁴, A. Branca⁹⁷, A. Brandt¹⁹³, J. Bremer³⁶, D. Breton¹⁵⁸, C. Brew¹⁷⁵, S. J. Brice⁶⁷, C. Brizzolari^{97,139}, C. Bromberg¹³⁸, J. Brooke²⁰, A. Bross⁶⁷, G. Brunetti^{97,139}, M. Brunetti²⁰⁴, N. Buchanan⁴⁵, H. Budd¹⁷², I. Butorov¹¹⁵, I. Cagnoli^{18,92}, T. Cai²¹¹, D. Caiulo¹⁰⁸, R. Calabrese^{68,94}, P. Calafiura¹²⁵, J. Calcutt¹⁵³, M. Calin²², S. Calvez⁴⁵, E. Calvo⁴⁰, A. Caminata⁹⁵, M. Campanelli¹⁹⁹, D. Caratelli⁶⁷, D. Carber⁴⁵, J. C. Carceller¹⁹⁹, G. Carini²¹, B. Carlus¹⁰⁸, M. F. Carneiro²¹, P. Carniti⁹⁷, I. Caro Terrazas⁴⁵, H. Carranza¹⁹³, T. Carroll²⁰⁸, J. F. Castaño Forero⁶, A. Castillo¹⁷⁸, C. Castromonte¹⁰³, E. Catano-Mur²⁰⁷, C. Cattadori⁹⁷, F. Cavalier¹⁵⁸, G. Cavallaro⁹⁷, F. Cavanna⁶⁷, S. Centro^{100,156}, G. Cerati⁶⁷, A. Cervelli⁹², A. Cervera Villanueva⁸⁵, M. Chalifour³⁶, A. Chappell²⁰⁴, E. Chardonnet¹⁵⁹, N. Charitonidis³⁶, A. Chatterjee¹⁶⁶, S. Chattopadhyay²⁰¹, M. S. S. Chavarry Neyra¹⁰³, H. Chen²¹, M. Chen²⁵, Y. Chen¹⁵, Z. Chen¹⁸⁵, Z. Chen-Wishart¹⁷³, Y. Cheon¹⁹⁸, D. Cherdack⁸¹, C. Chi⁴⁶, S. Childress⁶⁷, R. Chirco⁸⁷, A. Chiriacescu²², G. Chisnall¹⁸⁸, K. Cho¹²⁰, S. Choate¹⁴⁸, D. Chokheli⁷², P. S. Chong¹⁶², A. Christensen⁴⁵, D. Christian⁶⁷, G. Christodoulou³⁶, A. Chukanov¹¹⁵, M. Chung¹⁹⁸, E. Church¹⁵⁵, V. Cicero^{18,92}, P. Clarke⁵⁸, G. Cline¹²⁵, T. E. Coan¹⁸⁴, A. G. Cocco⁹⁹, J. A. B. Coelho¹⁵⁹, N. Colton⁴⁵, E. Conley⁵⁶, R. Conley¹⁸⁰, J. Conrad¹³⁴, M. Convery¹⁸⁰, S. Copello⁹⁵, P. Cova^{98,160}, L. Cremaldi¹⁴³, L. Cremonesi¹⁷⁰, J. I. Crespo-Anadón⁴⁰, M. Crisler⁶⁷, E. Cristaldo⁹, J. Crnkovic¹⁴³, R. Cross¹²⁴, A. Cudd⁴⁴, C. Cuesta^{40,a}, Y. Cui²⁷, D. Cussans²⁰, O. Dalager²⁵, H. da Motta³⁴, L. Da Silva Peres⁶⁶, C. David^{67,211}, Q. David¹⁰⁸, G. S. Davies¹⁴³, S. Davini⁹⁵, J. Dawson¹⁵⁹, K. De¹⁹³, S. De², P. Debbins¹⁰⁶, I. De Bonis⁵³, M. P. Decowski^{3,146}, A. De Gouvêa¹⁴⁹, P. C. De Holanda³¹, I. L. De Icaza Astiz¹⁸⁸, A. Deisting¹⁷³, P. De Jong^{3,146}, A. Delbart³⁵, D. Delepine⁷⁷, M. Delgado^{97,139}, A. Dell'Acqua³⁶, N. Delmonte^{98,160}, P. De Lurgio⁷, J. R. T. de Mello Neto⁶⁶, D. M. DeMuth²⁰⁰, S. Dennis³⁰, C. Densham¹⁷⁵, G. W. Deptuch²¹, A. De Roeck³⁶, V. De Romeri⁸⁵, G. De Souza³¹, R. Devi¹¹², R. Dharmapalan⁸⁰, M. Dias¹⁹⁷, F. Diaz¹⁶⁷, J. S. Díaz⁹¹, S. Di Domizio^{71,95}, L. Di Giulio³⁶, P. Ding⁶⁷, L. Di Noto^{71,95}, G. Dirx⁸⁸, C. Distefano¹⁰², R. Diurba¹⁴², M. Diwan²¹, Z. Djurcic⁷, D. Doering¹⁸⁰, S. Dolan³⁶, F. Dolek¹⁶, M. Dolinski⁵⁵, L. Domine¹⁸⁰, Y. Donon³⁶, D. Douglas¹³⁸, D. Douillet¹⁵⁸, A. Dragone¹⁸⁰, G. Drake⁶⁷, F. Drielsma¹⁸⁰, L. Duarte¹⁹⁷, D. Duchesneau⁵³, K. Duffy⁶⁷, P. Dunne⁸⁸, B. Dutta¹⁹¹, H. Duyang¹⁸¹, O. Dvornikov⁸⁰,

D. Dwyer¹²⁵, A. Dyshkant¹⁴⁸, M. Eads¹⁴⁸, A. Earle¹⁸⁸, D. Edmunds¹³⁸, J. Eisch⁶⁷, L. Emberger^{133,135}, S. Emery³⁵, P. Englezos¹⁷⁴, A. Ereditato²⁰⁹, T. Erjavec²⁴, C. Escobar⁶⁷, G. Eurin³⁵, J. J. Evans¹³³, E. Ewart⁹¹, A. C. Ezeribe¹⁷⁹, K. Fahey⁶⁷, A. Falcone^{97,139}, M. Fani¹²⁸, C. Farnese¹⁰⁰, Y. Farzan¹⁰⁹, D. Fedoseev¹¹⁵, J. Felix⁷⁷, Y. Feng¹⁰⁷, E. Fernandez-Martinez¹³¹, P. Fernandez Menendez⁸⁵, M. Fernandez Morales⁸⁶, F. Ferraro^{71,95}, L. Fields¹⁵⁰, P. Filip⁴⁹, F. Filthaut^{146,171}, M. Fiorini^{68,94}, V. Fischer¹⁰⁷, R. S. Fitzpatrick¹³⁷, W. Flanagan⁵², B. Fleming²⁰⁹, R. Flight¹⁷², S. Fogarty⁴⁵, W. Foreman⁸⁷, J. Fowler⁵⁶, W. Fox⁹¹, J. Franc⁵⁰, K. Francis¹⁴⁸, D. Franco²⁰⁹, J. Freeman⁶⁷, J. Freestone¹³³, J. Fried²¹, A. Friedland¹⁸⁰, F. Fuentes Robayo²⁰, S. Fuess⁶⁷, I. K. Furic⁶⁹, K. Furman¹⁷⁰, A. P. Furmanski¹⁴², A. Gabrielli⁹², A. Gago¹⁶⁷, H. Gallagher¹⁹⁶, A. Gallas¹⁵⁸, A. Gallego-Ros⁴⁰, N. Gallice^{98,140}, V. Galymov¹⁰⁸, E. Gamberini³⁶, T. Gamble¹⁷⁹, F. Ganacim¹⁹⁰, R. Gandhi⁷⁸, R. Gandrajula¹³⁸, F. Gao¹⁶⁶, S. Gao²¹, D. Garcia-Gamez⁷³, M. Á. García-Peris⁸⁵, S. Gardiner⁶⁷, D. Gastler¹⁹, J. Gauvreau¹⁵¹, G. Ge⁴⁶, N. Geffroy⁵³, B. Gelli³¹, A. Gendotti⁶⁰, S. Gent¹⁸³, Z. Ghorbani-Moghaddam⁹⁵, P. Giammaria³¹, T. Giammaria^{68,94}, N. Giangiacomi¹⁹⁵, D. Gibin^{100,156}, I. Gil-Botella⁴⁰, S. Gilligan¹⁵³, C. Girerd¹⁰⁸, A. K. Giri⁹⁰, D. Gnani¹²⁵, O. Gogota¹²³, M. Gold¹⁴⁴, S. Gollapinni¹²⁸, K. Gollwitzer⁶⁷, R. A. Gomes⁶³, L. V. Gomez Bermeo¹⁷⁸, L. S. Gomez Fajardo¹⁷⁸, F. Gonnella¹⁷, D. Gonzalez-Diaz⁸⁶, M. Gonzalez-Lopez¹³¹, M. C. Goodman⁷, O. Goodwin¹³³, S. Goswami¹⁶⁴, C. Gotti⁹⁷, E. Goudzovski¹⁷, C. Grace¹²⁵, R. Gran¹⁴¹, E. Granados⁷⁷, P. Granger³⁵, A. Grant⁵⁴, C. Grant¹⁹, D. Gratieri⁷⁰, P. Green¹³³, L. Greenler²⁰⁸, J. Greer²⁰, J. Grenard³⁶, W. C. Griffith¹⁸⁸, M. Groh⁴⁵, J. Grudzinski⁷, K. Grzelak²⁰³, W. Gu²¹, E. Guardincerri¹²⁸, V. Guarino⁷, M. Guarise^{68,94}, R. Guenette⁷⁹, E. Guerard¹⁵⁸, M. Guerzoni⁹², D. Guffanti⁹⁸, A. Guglielmi¹⁰⁰, B. Guo¹⁸¹, A. Gupta¹⁸⁰, V. Gupta¹⁴⁶, K. K. Guthikonda¹²¹, R. Gutierrez⁶, P. Guzowski¹³³, M. M. Guzzo³¹, S. Gwon³⁹, C. Ha³⁹, K. Haaf⁶⁷, A. Habig¹⁴¹, H. Hadavand¹⁹³, R. Haenni¹⁵, A. Hahn⁶⁷, J. Haiston¹⁸², P. Hamacher-Baumann¹⁵⁴, T. Hamernik⁶⁷, P. Hamilton⁸⁸, J. Han¹⁶⁶, D. A. Harris^{67,211}, J. Hartnell¹⁸⁸, T. Hartnett¹⁷⁵, J. Harton⁴⁵, T. Hasegawa¹¹⁹, C. Hasnip¹⁵⁴, R. Hatcher⁶⁷, K. W. Hatfield²⁵, A. Hatzikoutelis¹⁷⁷, C. Hayes⁹¹, K. Hayrapetyan¹⁷⁰, J. Hays¹⁷⁰, E. Hazen¹⁹, M. He⁸¹, A. Heavey⁶⁷, K. M. Heeger²⁰⁹, J. Heise¹⁸⁷, S. Henry¹⁷², M. A. Hernandez Morquecho⁸⁷, K. Herner⁶⁷, J. Hewes⁴¹, C. Hilgenberg¹⁴², T. Hill⁸³, S. J. Hillier¹⁷, A. Himmel⁶⁷, E. Hinkle³⁸, L. R. Hirsch¹⁹⁰, J. Ho⁷⁹, J. Hoff⁶⁷, A. Holin¹⁷⁵, E. Hoppe¹⁵⁵, G. A. Horton-Smith¹¹⁷, M. Hostert¹⁴², A. Hourlier¹³⁴, B. Howard⁶⁷, R. Howell¹⁷², J. Hoyos¹³⁶, I. Hristova¹⁷⁵, M. S. Hronek⁶⁷, J. Huang²⁴, Z. Hulcher¹⁸⁰, G. Iles⁸⁸, N. Ilic¹⁹⁵, A. M. Iliescu⁹², R. Illingworth⁶⁷, G. Ingrassia^{18,92}, A. Ioannisian²¹⁰, B. Irwin¹⁴², L. Isenhower¹, R. Itay¹⁸⁰, C. M. Jackson¹⁵⁵, V. Jain², E. James⁶⁷, W. Jang¹⁹³, B. Jargowsky²⁵, F. Jediny⁵⁰, D. Jena⁶⁷, Y. S. Jeong^{39,106}, C. Jesús-Valls⁸⁴, X. Ji²¹, L. Jiang²⁰², S. Jiménez⁴⁰, A. Jipa²², R. Johnson⁴¹, W. Johnson¹⁸², N. Johnston⁹¹, B. Jones¹⁹³, S. Jones¹⁹⁹, M. Judah¹⁶⁶, C. K. Jung¹⁸⁵, T. Junk⁶⁷, Y. Jwa⁴⁶, M. Kabirnezhad¹⁵⁴, A. Kaboth^{173,175}, I. Kadenko¹²³, I. Kakorin¹¹⁵, A. Kalitkina¹¹⁵, D. Kalra⁴⁶, F. Kamiya⁶⁵, N. Kaneshige²⁸, D. M. Kaplan⁸⁷, G. Karagiorgi⁴⁶, G. Karaman¹⁰⁶, A. Karcher¹²⁵, M. Karolak³⁵, Y. Karyotakis⁵³, S. Kasai¹²², S. P. Kasetti¹²⁹, L. Kashur⁴⁵, N. Kazaryan²¹⁰, E. Kearns¹⁹, P. Keener¹⁶², K. J. Kelly³⁶, E. Kemp³¹, O. Kemularia⁷², W. Ketchum⁶⁷, S. H. Kettell²¹, M. Khabibullin¹⁰⁴, A. Khotjantsev¹⁰⁴, A. Khvedelidze⁷², D. Kim¹⁹¹, B. King⁶⁷, B. Kirby⁴⁶, M. Kirby⁶⁷, J. Klein¹⁶², A. Klustova⁸⁸, T. Kobilarcik⁶⁷, K. Koehler²⁰⁸, L. W. Koerner⁸¹, D. H. Koh¹⁸⁰, S. Kohn^{23,125}, P. P. Koller¹⁵, L. Kolupaeva¹¹⁵, D. Korablev¹¹⁵, M. Kordosky²⁰⁷, T. Kosc⁷⁶, U. Kose³⁶, V. A. Kostecký⁹¹, K. Kotheke²⁰, R. Kralik¹⁸⁸, L. Kreczko²⁰, F. Krennrich¹⁰⁷, I. Kreslo¹⁵, W. Kropp²⁵, T. Kroupova¹⁶², S. Kubota⁷⁹, Y. Kudenko¹⁰⁴, V. A. Kudryavtsev¹⁷⁹, S. Kulagin¹⁰⁴, J. Kumar⁸⁰, P. Kumar¹⁷⁹, P. Kunze⁵³, N. Kurita¹⁸⁰, C. Kuruppu¹⁸¹, V. Kus⁵⁰, T. Kutter¹²⁹, J. Kvasnicka⁴⁹, D. Kwak¹⁹⁸, A. Lambert¹²⁵, B. Land¹⁶², C. E. Lane⁵⁵, K. Lang¹⁹⁴, T. Langford²⁰⁹, M. Langstaff¹³³, J. Larkin²¹, P. Lasorak¹⁸⁸, D. Last¹⁶², A. Laundrie²⁰⁸, G. Laurenti⁹², A. Lawrence¹²⁵, I. Lazanu²², R. LaZur⁴⁵, M. Lazzaroni^{98,140}, T. Le¹⁹⁶, S. Leardini⁸⁶, J. Learned⁸⁰, P. LeBrun¹⁰⁸, T. LeCompte¹⁸⁰, C. Lee⁶⁷, S. Y. Lee¹¹⁴, G. Lehmann Miotto³⁶, R. Lehnert⁹¹, M. A. Leigui de Oliveira⁶⁵, M. Leitner¹²⁵, L. M. Lepin¹³³, S. W. Li¹⁸⁰, Y. Li²¹, H. Liao¹¹⁷, C. S. Lin¹²⁵, Q. Lin¹⁸⁰, S. Lin¹²⁹, R. A. Lineros³³, J. Ling¹⁸⁶, A. Lister²⁰⁸, B. R. Littlejohn⁸⁷, J. Liu²⁵, Y. Liu³⁸, S. Lockwitz⁶⁷, T. Loew¹²⁵, M. Lokajicek⁴⁹, I. Lomidze⁷², K. Long⁸⁸, T. Lord²⁰⁴, J. M. LoSecco¹⁵⁰, W. C. Louis¹²⁸, X.-G. Lu²⁰⁴, K. B. Luk^{23,125}, B. Lunday¹⁶², X. Luo²⁸, E. Luppi^{68,94}, T. Lux⁸⁴, V. P. Luzio⁶⁵, J. Maalmi¹⁵⁸, D. MacFarlane¹⁸⁰, A. A. Machado³¹, P. Machado⁶⁷, C. T. Macias⁹¹, J. R. Macier⁶⁷, A. Maddalena⁷⁵, A. Madera³⁶, P. Madigan^{23,125}, S. Magill⁷, K. Mahn¹³⁸, A. Maio^{61,126}, A. Major⁵⁶, J. A. Maloney⁵¹, G. Mandrioli⁹², R. C. Mandujano²⁵, J. Maneira^{61,126}, L. Manenti¹⁹⁹, S. Manly¹⁷², A. Mann¹⁹⁶, K. Manolopoulos¹⁷⁵, M. Manrique Plata⁹¹, V. N. Manyam²¹, L. Manzanillas¹⁵⁸, M. Marchan⁶⁷, A. Marchionni⁶⁷, W. Marciano²¹, D. Marfatia⁸⁰, C. Mariani²⁰², J. Maricic⁸⁰, R. Marie¹⁵⁸, F. Marinho⁶⁴, A. D. Marino⁴⁴, D. Marsden¹³³, M. Marshak¹⁴², C. Marshall¹⁷², J. Marshall²⁰⁴, J. Marteau¹⁰⁸, J. Martín-Albo⁸⁵, N. Martínez¹¹⁷, D. A. Martínez Caicedo¹⁸², P. Martínez Miravé⁸⁵, S. Martynenko¹⁸⁵, V. Mascagna^{97,105}, K. Mason¹⁹⁶, A. Mastbaum¹⁷⁴, F. Matichard¹²⁵, S. Matsuno⁸⁰, J. Matthews¹²⁹, C. Mauger¹⁶², N. Mauri^{18,92}, K. Mavrokoridis¹²⁷,

I. Mawby²⁰⁴, R. Mazza⁹⁷, A. Mazzacane⁶⁷, E. Mazzucato³⁵, T. McAskill²⁰⁵, E. McCluskey⁶⁷, N. McConkey¹³³, K. S. McFarland¹⁷², C. McGrew¹⁸⁵, A. McNab¹³³, A. Mefodiev¹⁰⁴, P. Mehta¹¹³, P. Melas¹⁰, O. Mena⁸⁵, H. Mendez¹⁶⁸, P. Mendez³⁶, D. P. Méndez²¹, A. Menegolli^{101,161}, G. Meng¹⁰⁰, M. D. Messier⁹¹, W. Metcalf¹²⁹, T. Mettler¹⁵, M. Mewes⁹¹, H. Meyer²⁰⁶, T. Miao⁶⁷, G. Michna¹⁸³, T. Miedema^{146,171}, V. Mikola¹⁹⁹, R. Milincic⁸⁰, G. Miller¹³³, W. Miller¹⁴², J. Mills¹⁹⁶, O. Mineev¹⁰⁴, A. Minotti^{98,139}, O. G. Miranda⁴², S. Miryala²¹, C. S. Mishra⁶⁷, S. R. Mishra¹⁸¹, A. Mislivec¹⁴², M. Mitchell¹²⁹, D. Mladenov³⁶, I. Mocioiu¹⁶³, K. Moffat⁵⁷, N. Moggi^{18,92}, R. Mohanta⁸², T. A. Mohayai⁶⁷, N. Mokhov⁶⁷, J. Molina⁹, L. Molina Bueno⁸⁵, E. Montagna^{18,92}, A. Montanari⁹², C. Montanari^{67,101,161}, D. Montanari⁶⁷, L. M. Montaña Zetina⁴², S. H. Moon¹⁹⁸, M. Mooney⁴⁵, A. F. Moor³⁰, D. Moreno⁶, D. Moretti⁹⁷, C. Morris⁸¹, C. Mossey⁶⁷, M. Mote¹²⁹, E. Motuk¹⁹⁹, C. A. Moura⁶⁵, J. Mousseau¹³⁷, G. Moustier¹²⁴, W. Mu⁶⁷, L. Muallem²⁹, J. Mueller⁴⁵, M. Muether²⁰⁶, S. Mufson⁹¹, F. Muheim⁵⁸, A. Muir⁵⁴, M. Mulhearn²⁴, D. Munford⁸¹, H. Muramatsu¹⁴², S. Murphy⁶⁰, J. Musser⁹¹, J. Nachtman¹⁰⁶, S. Nagu¹³⁰, M. Nalbandyan²¹⁰, R. Nandakumar¹⁷⁵, D. Naples¹⁶⁶, S. Narita¹¹¹, A. Nath⁸⁹, A. Navrer-Agasson¹³³, N. Nayak²⁵, M. Nebot-Guinot⁵⁸, K. Negishi¹¹¹, J. K. Nelson²⁰⁷, J. Nesbit²⁰⁸, M. Nessi³⁶, D. Newbold¹⁷⁵, M. Newcomer¹⁶², H. Newton⁵⁴, R. Nichol¹⁹⁹, F. Nicolas-Arnaldos⁷³, A. Nikolica¹⁶², E. Niner⁶⁷, K. Nishimura⁸⁰, A. Norman⁶⁷, A. Norrick⁶⁷, R. Northrop³⁸, P. Novella⁸⁵, J. A. Nowak¹²⁴, M. Oberling⁷, J. Ochoa-Ricoux²⁵, A. Olivier¹⁷², A. Olshevskiy¹¹⁵, Y. Onel¹⁰⁶, Y. Onishchuk¹²³, J. Ott²⁵, L. Pagani²⁴, G. Palacio⁵⁹, O. Palamara⁶⁷, S. Palestini³⁶, J. M. Paley⁶⁷, M. Pallavicini^{71,95}, C. Palomares⁴⁰, W. Panduro Vazquez¹⁷³, E. Pantic²⁴, V. Paolone¹⁶⁶, V. Papadimitriou⁶⁷, R. Papaleo¹⁰², A. Papanestis¹⁷⁵, S. Paramesvaran²⁰, S. Parke⁶⁷, E. Parozzi^{97,139}, Z. Parsa²¹, M. Parvu²², S. Pascoli^{18,57}, L. Pasqualini^{18,92}, J. Pasternak⁸⁸, J. Pater¹³³, C. Patrick¹⁹⁹, L. Patrizzii⁹², R. B. Patterson²⁹, S. J. Patton¹²⁵, T. Patzak¹⁵⁹, A. Paudel⁶⁷, B. Paulos²⁰⁸, L. Paulucci⁶⁵, Z. Pavlovic⁶⁷, G. Pawloski¹⁴², D. Payne¹²⁷, V. Pec⁴⁹, S. J. M. Peeters¹⁸⁸, A. Pena Perez¹⁸⁰, E. Pennacchio¹⁰⁸, A. Penzo¹⁰⁶, O. L. G. Peres³¹, J. Perry⁵⁸, D. Pershey⁵⁶, G. Pessina⁹⁷, G. Petrillo¹⁸⁰, C. Petta^{32,93}, R. Petti¹⁸¹, V. Pia^{18,92}, F. Piastra¹⁵, L. Pickering¹³⁸, F. Pietropaolo^{36,100}, V. L. Pimentel^{31,47}, G. Pinaroli²¹, K. Plows¹⁵⁴, R. Plunkett⁶⁷, R. Poling¹⁴², F. Pompa⁸⁵, X. Pons³⁶, N. Poonthottathil¹⁰⁷, F. Poppi^{18,92}, S. Pordes⁶⁷, J. Porter¹⁸⁸, M. Potekhin²¹, R. Potenza^{32,93}, B. V. K. S. Potukuchi¹¹², J. Pozimski⁸⁸, M. Pozzato^{18,92}, S. Prakash³¹, T. Prakash¹²⁵, M. Prest⁹⁷, S. Prince⁷⁹, F. Psihas⁶⁷, D. Pugnere¹⁰⁸, X. Qian²¹, J. L. Raaf⁶⁷, V. Radeka²¹, J. Rademacker²⁰, B. Radics⁶⁰, A. Rafique⁷, E. Raguzin²¹, M. Rai²⁰⁴, M. Rajaoalisoa⁴¹, I. Rakhno⁶⁷, A. Rakotonandrasana⁵, L. Rakotondravohitra⁵, R. Rameika⁶⁷, M. A. Ramirez Delgado¹⁶², B. Ramson⁶⁷, A. Rappoldi^{101,161}, G. Raselli^{101,161}, P. Ratoff¹²⁴, S. Raut¹⁸⁵, R. F. Razakamiandra⁵, E. M. Rea¹⁴², J. S. Real⁷⁶, B. Rebel^{67,208}, R. Rechenmacher⁶⁷, M. Reggiani-Guzzo¹³³, J. Reichenbacher¹⁸², S. D. Reitzner⁶⁷, H. Rejeb Sfar³⁶, A. Renshaw⁸¹, S. Rescia²¹, F. Resnati³⁶, M. Ribas¹⁹⁰, S. Riboldi⁹⁸, C. Riccio¹⁸⁵, G. Riccobene¹⁰², L. C. J. Rice¹⁶⁶, J. S. Ricol⁷⁶, A. Rigamonti³⁶, Y. Rigaut⁶⁰, E. V. Rincón⁵⁹, H. Ritchie-Yates¹⁷³, D. Rivera¹²⁸, A. Robert⁷⁶, L. Rochester¹⁸⁰, M. Roda¹²⁷, P. Rodrigues¹⁵⁴, M. J. Rodriguez Alonso³⁶, E. Rodriguez Bonilla⁶, J. Rodriguez Rondon¹⁸², S. Rosauro-Alcaraz¹³¹, M. Rosenberg¹⁶⁶, P. Rosier¹⁵⁸, B. Roskovec²⁵, M. Rossella^{101,161}, M. Rossi³⁶, J. Rout¹¹³, P. Roy²⁰⁶, A. Rubbia⁶⁰, C. Rubbia⁷⁴, B. Russell¹²⁵, D. Ruterbories¹⁷², A. Rybnikov¹¹⁵, A. Saa-Hernandez⁸⁶, R. Saakyan¹⁹⁹, S. Sacerdoti¹⁵⁹, T. Safford¹³⁸, N. Sahu⁹⁰, K. Sakashita¹¹⁹, P. Sala^{36,98}, N. Samios²¹, O. Samoylov¹¹⁵, M. C. Sanchez¹⁰⁷, V. Sandberg¹²⁸, D. A. Sanders¹⁴³, D. Sankey¹⁷⁵, S. Santana¹⁶⁸, M. Santos-Maldonado¹⁶⁸, N. Saoulidou¹⁰, P. Sapienza¹⁰², C. Sarasty⁴¹, I. Sarcevic⁸, G. Savage⁶⁷, V. Savinov¹⁶⁶, A. Scaramelli¹⁰¹, A. Scarff¹⁷⁹, A. Scarpelli²¹, T. Schefke¹²⁹, H. Schellman^{67,153}, S. Schifano^{68,94}, P. Schlabach⁶⁷, D. Schmitz³⁸, A. W. Schneider¹³⁴, K. Scholberg⁵⁶, A. Schukraft⁶⁷, E. Segreto³¹, A. Selyunin¹¹⁵, C. R. Senise Jr.¹⁹⁷, J. Sensenig¹⁶², A. Sergi¹⁷, D. Sgalaberna⁶⁰, M. H. Shaevitz⁴⁶, S. Shafaq¹¹³, F. Shaker²¹¹, M. Shamma²⁷, R. Sharankova¹⁹⁶, H. R. Sharma¹¹², R. Sharma²¹, R. K. Sharma¹⁶⁹, T. Shaw⁶⁷, K. Shchablo¹⁰⁸, C. Shepherd-Themistocleous¹⁷⁵, A. Sheshukov¹¹⁵, S. Shin¹¹⁴, I. Shoemaker²⁰², D. Shooltz¹³⁸, R. Shrock¹⁸⁵, H. Siegel⁴⁶, L. Simard¹⁵⁸, J. Sinclair¹⁸⁰, G. Sinev¹⁸², J. Singh¹³⁰, J. Singh¹³⁰, L. Singh⁴⁸, P. Singh¹⁷⁰, V. Singh^{13,48}, R. Sipoš³⁶, F. W. Sippach⁴⁶, G. Sirri⁹², A. Sitiraka¹⁸², K. Siyeon³⁹, K. Skarpaas¹⁸⁰, A. Smith³⁰, E. Smith⁹¹, P. Smith⁹¹, J. Smolik⁵⁰, M. Smy²⁵, E. Snider⁶⁷, P. Snopok⁸⁷, D. Snowden-Ifft¹⁵¹, M. Soares Nunes¹⁸⁹, H. Sobel²⁵, M. Soderberg¹⁸⁹, S. Sokolov¹¹⁵, C. J. Solano Salinas¹⁰³, S. Söldner-Rembold¹³³, S. R. Soleti¹²⁵, N. Solomey²⁰⁶, V. Solovov¹²⁶, W. E. Sondheim¹²⁸, M. Sorel⁸⁵, A. Sotnikov¹¹⁵, J. Soto-Oton⁴⁰, F. A. Soto Ugaldí¹⁰³, A. Sousa⁴¹, K. Soustruznik³⁷, F. Spaggiardi¹⁵⁴, M. Spanu^{97,139}, J. Spitz¹³⁷, N. J. C. Spooner¹⁷⁹, K. Spurgeon¹⁸⁹, M. Stancari⁶⁷, L. Stanco^{100,156}, C. Stanford⁷⁹, R. Stein²⁰, H. M. Steiner¹²⁵, A. F. Steklain Lisboa¹⁹⁰, J. Stewart²¹, B. Stillwell³⁸, J. Stock¹⁸², F. Stocker³⁶, T. Stokes¹²⁹, M. Strait¹⁴², T. Strauss⁶⁷, L. Strigari¹⁹¹, A. Stuart⁴³, J. G. Suarez⁵⁹, J. M. Suárez Sunció¹⁰³, H. Sullivan¹⁹³, D. Summers¹⁴³, A. Surdo⁹⁶, V. Susic¹⁴, L. Suter⁶⁷, C. M. Sutura^{32,93}, R. Svoboda²⁴, B. Szczerbinska¹⁹², A. M. Szelc⁵⁸, H. Tanaka¹⁸⁰, S. Tang²¹, A. Tapia¹³⁶, B. Tapia Oregui¹⁹⁴, A. Tapper⁸⁸, S. Tariq⁶⁷, E. Tarpara²¹, N. Tata⁷⁹, E. Tatar⁸³, R. Tayloe⁹¹

A. M. Teklu¹⁸⁵, P. Tennessen^{4,125}, M. Tenti⁹², K. Terao¹⁸⁰, C. A. Ternes⁸⁵, F. Terranova^{97,139}, G. Testera⁹⁵, T. Thakore⁴¹, A. Thea¹⁷⁵, J. L. Thompson¹⁷⁹, C. Thorn²¹, S. C. Timm⁶⁷, V. Tishchenko²¹, L. Tomassetti^{68,94}, A. Tonazzo¹⁵⁹, D. Torbunov¹⁴², M. Torti^{97,139}, M. Tortola⁸⁵, F. Tortorici^{32,93}, N. Tosi⁹², D. Totani²⁸, M. Touns⁶⁷, C. Touramanis¹²⁷, R. Travaglini⁹², J. Trevor²⁹, S. Trilov²⁰, W. H. Trzaska¹¹⁶, Y. Tsai²⁵, Y.-T. Tsai¹⁸⁰, Z. Tsamalaidze⁷², K. V. Tsang¹⁸⁰, N. Tsverava⁷², S. Tufanli³⁶, C. Tull¹²⁵, E. Tyley¹⁷⁹, M. Tzanov¹²⁹, L. Uboldi³⁶, M. A. Uchida³⁰, J. Urheim⁹¹, T. Usher¹⁸⁰, S. Uzunyan¹⁴⁸, M. R. Vagins¹¹⁸, P. Vahle²⁰⁷, S. Valder¹⁸⁸, G. D. A. Valdivieso⁶², E. Valencia⁷⁷, R. Valentim¹⁹⁷, Z. Vallari²⁹, E. Vallazza⁹⁷, J. W. F. Valle⁸⁵, S. Vallecorsa³⁶, R. Van Berg¹⁶², R. G. Van de Water¹²⁸, D. Vanegas Forero¹³⁶, D. Vannerom¹³⁴, F. Varanini¹⁰⁰, D. Vargas Oliva⁸⁴, G. Varner⁸⁰, J. Vasel⁹¹, S. Vasina¹¹⁵, G. Vasseur³⁵, N. Vaughan¹⁵³, K. Vaziri⁶⁷, S. Ventura¹⁰⁰, A. Verdugo⁴⁰, S. Vergani³⁰, M. A. Vermeulen¹⁴⁶, M. Verzocchi⁶⁷, M. Vicenzi^{71,95}, H. Vieira de Souza¹⁵⁹, C. Vignoli⁷⁵, C. Vilela³⁶, B. Viren²¹, T. Vrba⁵⁰, T. Wachala¹⁴⁵, A. V. Waldron⁸⁸, M. Wallbank⁴¹, C. Wallis⁴⁵, H. Wang²⁶, J. Wang¹⁸², L. Wang¹²⁵, M. H. L. S. Wang⁶⁷, X. Wang⁶⁷, Y. Wang²⁶, Y. Wang¹⁸⁵, K. Warburton¹⁰⁷, D. Warner⁴⁵, M. O. Wascko⁸⁸, D. Waters¹⁹⁹, A. Watson¹⁷, K. Wawrowska^{175,188}, P. Weatherly⁵⁵, A. Weber^{67,132}, M. Weber¹⁵, H. Wei²¹, A. Weinstein¹⁰⁷, D. Wenman²⁰⁸, M. Wetstein¹⁰⁷, A. White¹⁹³, L. H. Whitehead³⁰, D. Whittington¹⁸⁹, M. J. Wilking¹⁸⁵, A. Wilkinson¹⁹⁹, C. Wilkinson¹²⁵, Z. Williams¹⁹³, F. Wilson¹⁷⁵, R. J. Wilson⁴⁵, W. Wisniewski¹⁸⁰, J. Wolcott¹⁹⁶, T. Wongjirad¹⁹⁶, A. Wood⁸¹, K. Wood¹²⁵, E. Worcester²¹, M. Worcester²¹, K. Wresilo³⁰, C. Wret¹⁷², W. Wu⁶⁷, W. Wu²⁵, Y. Xiao²⁵, F. Xie¹⁸⁸, B. Yaeggy⁴¹, E. Yandel²⁸, G. Yang¹⁸⁵, K. Yang¹⁵⁴, T. Yang⁶⁷, A. Yankelevich²⁵, N. Yershov¹⁰⁴, K. Yonehara⁶⁷, Y. S. Yoon³⁹, T. Young¹⁴⁷, B. Yu²¹, H. Yu²¹, H. Yu¹⁸⁶, J. Yu¹⁹³, Y. Yu⁸⁷, W. Yuan⁵⁸, R. Zaki²¹¹, J. Zalesak⁴⁹, L. Zambelli⁵³, B. Zamorano⁷³, A. Zani⁹⁸, L. Zazueta²⁰⁷, G. P. Zeller⁶⁷, J. Zennaro⁶⁷, K. Zeug²⁰⁸, C. Zhang²¹, S. Zhang⁹¹, Y. Zhang¹⁶⁶, M. Zhao²¹, E. Zhivun²¹, G. Zhu¹⁵², E. D. Zimmerman⁴⁴, S. Zucchelli^{18,92}, J. Zuklin⁴⁹, V. Zutshi¹⁴⁸, R. Zwaska⁶⁷

¹ Abilene Christian University, Abilene, TX 79601, USA

² University of Albany, SUNY, Albany, NY 12222, USA

³ University of Amsterdam, 1098 XG Amsterdam, The Netherlands

⁴ Antalya Bilim University, 07190 Döşemealti/Antalya, Turkey

⁵ University of Antananarivo, 101 Antananarivo, Madagascar

⁶ Universidad Antonio Nariño, Bogotá, Colombia

⁷ Argonne National Laboratory, Argonne, IL 60439, USA

⁸ University of Arizona, Tucson, AZ 85721, USA

⁹ Universidad Nacional de Asunción, San Lorenzo, Paraguay

¹⁰ University of Athens, 157 84 Zografou, Greece

¹¹ Universidad del Atlántico, Barranquilla, Atlántico, Colombia

¹² Augustana University, Sioux Falls, SD 57197, USA

¹³ Banaras Hindu University, Varanasi 221 005, India

¹⁴ University of Basel, 4056 Basel, Switzerland

¹⁵ University of Bern, 3012 Bern, Switzerland

¹⁶ Beykent University, Istanbul, Turkey

¹⁷ University of Birmingham, Birmingham B15 2TT, UK

¹⁸ Università del Bologna, 40127 Bologna, Italy

¹⁹ Boston University, Boston, MA 02215, USA

²⁰ University of Bristol, Bristol BS8 1TL, UK

²¹ Brookhaven National Laboratory, Upton, NY 11973, USA

²² University of Bucharest, Bucharest, Romania

²³ University of California Berkeley, Berkeley, CA 94720, USA

²⁴ University of California Davis, Davis, CA 95616, USA

²⁵ University of California Irvine, Irvine, CA 92697, USA

²⁶ University of California Los Angeles, Los Angeles, CA 90095, USA

²⁷ University of California Riverside, Riverside, CA 92521, USA

²⁸ University of California Santa Barbara, Santa Barbara, CA 93106, USA

²⁹ California Institute of Technology, Pasadena, CA 91125, USA

³⁰ University of Cambridge, Cambridge CB3 0HE, UK

³¹ Universidade Estadual de Campinas, Campinas, SP 13083-970, Brazil

³² Università di Catania, 2, 95131 Catania, Italy

³³ Universidad Católica del Norte, Antofagasta, Chile

³⁴ Centro Brasileiro de Pesquisas Físicas, Rio de Janeiro, RJ 22290-180, Brazil

³⁵ IRFU, CEA, Université Paris-Saclay, 91191 Gif-sur-Yvette, France

³⁶ CERN, The European Organization for Nuclear Research, 1211 Meyrin, Switzerland

³⁷ Institute of Particle and Nuclear Physics of the Faculty of Mathematics and Physics of the Charles University, 180 00 Prague 8, Czech Republic

³⁸ University of Chicago, Chicago, IL 60637, USA

- 39 Chung-Ang University, Seoul 06974, South Korea
- 40 CIEMAT, Centro de Investigaciones Energéticas, Medioambientales y Tecnológicas, 28040 Madrid, Spain
- 41 University of Cincinnati, Cincinnati, OH 45221, USA
- 42 Centro de Investigación y de Estudios Avanzados del Instituto Politécnico Nacional (Cinvestav), Mexico City, Mexico
- 43 Universidad de Colima, Colima, Mexico
- 44 University of Colorado Boulder, Boulder, CO 80309, USA
- 45 Colorado State University, Fort Collins, CO 80523, USA
- 46 Columbia University, New York, NY 10027, USA
- 47 Centro de Tecnologia da Informacao Renato Archer, Amarais, Campinas, SP CEP 13069-901, Brazil
- 48 Central University of South Bihar, Gaya 824236, India
- 49 Institute of Physics, Czech Academy of Sciences, 182 00 Prague 8, Czech Republic
- 50 Czech Technical University, 115 19 Prague 1, Czech Republic
- 51 Dakota State University, Madison, SD 57042, USA
- 52 University of Dallas, Irving, TX 75062-4736, USA
- 53 Laboratoire d'Annee de Physique des Particules, Univ. Grenoble Alpes, Univ. Savoie Mont Blanc, CNRS, LAPP-IN2P3, 74000 Annecy, France
- 54 Daresbury Laboratory, Cheshire WA4 4AD, UK
- 55 Drexel University, Philadelphia, PA 19104, USA
- 56 Duke University, Durham, NC 27708, USA
- 57 Durham University, Durham DH1 3LE, UK
- 58 University of Edinburgh, Edinburgh EH8 9YL, UK
- 59 Universidad EIA, Envigado, Antioquia, Colombia
- 60 ETH Zurich, Zurich, Switzerland
- 61 Faculdade de Ciências da Universidade de Lisboa-FCUL, 1749-016 Lisbon, Portugal
- 62 Universidade Federal de Alfenas, Poços de Caldas, MG 37715-400, Brazil
- 63 Universidade Federal de Goiás, Goiania, GO 74690-900, Brazil
- 64 Universidade Federal de São Carlos, Araras, SP 13604-900, Brazil
- 65 Universidade Federal do ABC, Santo André, SP 09210-580, Brazil
- 66 Universidade Federal do Rio de Janeiro, Rio de Janeiro, RJ 21941-901, Brazil
- 67 Fermi National Accelerator Laboratory, Batavia, IL 60510, USA
- 68 University of Ferrara, Ferrara, Italy
- 69 University of Florida, Gainesville, FL 32611-8440, USA
- 70 Fluminense Federal University, 9 Icaraí, Niterói, RJ 24220-900, Brazil
- 71 Università degli Studi di Genova, Genoa, Italy
- 72 Georgian Technical University, Tbilisi, Georgia
- 73 University of Granada & CAFPE, 18002 Granada, Spain
- 74 Gran Sasso Science Institute, L'Aquila, Italy
- 75 Laboratori Nazionali del Gran Sasso, L'Aquila, AQ, Italy
- 76 University Grenoble Alpes, CNRS, Grenoble INP, LPSC-IN2P3, 38000 Grenoble, France
- 77 Universidad de Guanajuato, C.P. 37000 Guanajuato, Mexico
- 78 Harish-Chandra Research Institute, Jhansi, Allahabad 211 019, India
- 79 Harvard University, Cambridge, MA 02138, USA
- 80 University of Hawaii, Honolulu, HI 96822, USA
- 81 University of Houston, Houston, TX 77204, USA
- 82 University of Hyderabad, Gachibowli, Hyderabad 500 046, India
- 83 Idaho State University, Pocatello, ID 83209, USA
- 84 Institut de Física d'Altes Energies (IFAE)-Barcelona Institute of Science and Technology (BIST), Barcelona, Spain
- 85 Instituto de Física Corpuscular, CSIC and Universitat de València, 46980 Paterna, Valencia, Spain
- 86 Instituto Galego de Física de Altas Enerxias, A Coruña, Spain
- 87 Illinois Institute of Technology, Chicago, IL 60616, USA
- 88 Imperial College of Science Technology and Medicine, London SW7 2BZ, UK
- 89 Indian Institute of Technology Guwahati, Guwahati 781 039, India
- 90 Indian Institute of Technology Hyderabad, Hyderabad 502285, India
- 91 Indiana University, Bloomington, IN 47405, USA
- 92 Istituto Nazionale di Fisica Nucleare Sezione di Bologna, 40127 Bologna, BO, Italy
- 93 Istituto Nazionale di Fisica Nucleare Sezione di Catania, 95123 Catania, Italy
- 94 Istituto Nazionale di Fisica Nucleare Sezione di Ferrara, 44122 Ferrara, Italy
- 95 Istituto Nazionale di Fisica Nucleare Sezione di Genova, 16146 Genoa, GE, Italy
- 96 Istituto Nazionale di Fisica Nucleare Sezione di Lecce, 73100 Lecce, Italy
- 97 Istituto Nazionale di Fisica Nucleare Sezione di Milano Bicocca, 3, 20126 Milan, Italy
- 98 Istituto Nazionale di Fisica Nucleare Sezione di Milano, 20133 Milan, Italy
- 99 Istituto Nazionale di Fisica Nucleare Sezione di Napoli, 80126 Naples, Italy
- 100 Istituto Nazionale di Fisica Nucleare Sezione di Padova, 35131 Padua, Italy
- 101 Istituto Nazionale di Fisica Nucleare Sezione di Pavia, 27100 Pavia, Italy
- 102 Istituto Nazionale di Fisica Nucleare Laboratori Nazionali del Sud, 95123 Catania, Italy
- 103 Universidad Nacional de Ingeniería, Lima 25, Peru

- 104 Institute for Nuclear Research of the Russian Academy of Sciences, Moscow 117312, Russia
105 University of Insubria, Via Ravasi, 2, 21100 Varese, VA, Italy
106 University of Iowa, Iowa City, IA 52242, USA
107 Iowa State University, Ames, IA 50011, USA
108 Institut de Physique des 2 Infinis de Lyon, 69622 Villeurbanne, France
109 Institute for Research in Fundamental Sciences, Tehran, Iran
110 Instituto Superior Técnico-IST, Universidade de Lisboa, 1049-001 Lisbon, Portugal
111 Iwate University, Morioka, Iwate 020-8551, Japan
112 University of Jammu, Jammu 180006, India
113 Jawaharlal Nehru University, New Delhi 110067, India
114 Jeonbuk National University, Jeonrabuk-do 54896, South Korea
115 Joint Institute for Nuclear Research, Dzhelapov Laboratory of Nuclear Problems 6 Joliot-Curie, Dubna, Moscow Region 141980, Russia
116 University of Jyväskylä, 40014 Jyväskylä, Finland
117 Kansas State University, Manhattan, KS 66506, USA
118 Kavli Institute for the Physics and Mathematics of the Universe, Kashiwa, Chiba 277-8583, Japan
119 High Energy Accelerator Research Organization (KEK), Ibaraki 305-0801, Japan
120 Korea Institute of Science and Technology Information, Daejeon 34141, South Korea
121 K L University, Vaddeswaram, Andhra Pradesh 522502, India
122 National Institute of Technology, Kure College, Hiroshima 737-8506, Japan
123 Taras Shevchenko National University of Kyiv, Kyiv 01601, Ukraine
124 Lancaster University, Lancaster LA1 4YB, UK
125 Lawrence Berkeley National Laboratory, Berkeley, CA 94720, USA
126 Laboratório de Instrumentação e Física Experimental de Partículas, 1649-003 Lisboa, 3004-516 Coimbra, Portugal
127 University of Liverpool, Liverpool L69 7ZE, UK
128 Los Alamos National Laboratory, Los Alamos, NM 87545, USA
129 Louisiana State University, Baton Rouge, LA 70803, USA
130 University of Lucknow, Lucknow, Uttar Pradesh 226007, India
131 Madrid Autonoma University and IFT UAM/CSIC, 28049 Madrid, Spain
132 Johannes Gutenberg-Universität Mainz, 55122 Mainz, Germany
133 University of Manchester, Manchester M13 9PL, UK
134 Massachusetts Institute of Technology, Cambridge, MA 02139, USA
135 Max-Planck-Institut, 80805 Munich, Germany
136 University of Medellín, Medellín 050026, Colombia
137 University of Michigan, Ann Arbor, MI 48109, USA
138 Michigan State University, East Lansing, MI 48824, USA
139 Università del Milano-Bicocca, 20126 Milan, Italy
140 Università degli Studi di Milano, 20133 Milan, Italy
141 University of Minnesota Duluth, Duluth, MN 55812, USA
142 University of Minnesota Twin Cities, Minneapolis, MN 55455, USA
143 University of Mississippi, University, MS 38677, USA
144 University of New Mexico, Albuquerque, NM 87131, USA
145 H. Niewodniczański Institute of Nuclear Physics, Polish Academy of Sciences, Kraków, Poland
146 Nikhef National Institute of Subatomic Physics, 1098 XG Amsterdam, The Netherlands
147 University of North Dakota, Grand Forks, ND 58202-8357, USA
148 Northern Illinois University, DeKalb, IL 60115, USA
149 Northwestern University, Evanston, IL 60208, USA
150 University of Notre Dame, Notre Dame, IN 46556, USA
151 Occidental College, Los Angeles, CA 90041, USA
152 Ohio State University, Columbus, OH 43210, USA
153 Oregon State University, Corvallis, OR 97331, USA
154 University of Oxford, Oxford OX1 3RH, UK
155 Pacific Northwest National Laboratory, Richland, WA 99352, USA
156 Università degli Studi di Padova, 35131 Padua, Italy
157 Panjab University, Chandigarh, U.T. 160014, India
158 Université Paris-Saclay, CNRS/IN2P3, IJCLab, 91405 Orsay, France
159 Université de Paris, CNRS, Astroparticule et Cosmologie, 75006 Paris, France
160 University of Parma, 43121 Parma, PR, Italy
161 Università degli Studi di Pavia, 27100 Pavia, PV, Italy
162 University of Pennsylvania, Philadelphia, PA 19104, USA
163 Pennsylvania State University, University Park, PA 16802, USA
164 Physical Research Laboratory, Ahmedabad 380 009, India
165 Università di Pisa, 56127 Pisa, Italy
166 University of Pittsburgh, Pittsburgh, PA 15260, USA
167 Pontificia Universidad Católica del Perú, Lima, Peru
168 University of Puerto Rico, Mayaguez, PR 00681, USA
169 Punjab Agricultural University, Ludhiana 141004, India

- 170 Queen Mary University of London, London E1 4NS, UK
171 Radboud University, 6525 AJ Nijmegen, The Netherlands
172 University of Rochester, Rochester, NY 14627, USA
173 Royal Holloway College, London TW20 0EX, UK
174 Rutgers University, Piscataway, NJ 08854, USA
175 STFC Rutherford Appleton Laboratory, Didcot OX11 0QX, UK
176 Università del Salento, 73100 Lecce, Italy
177 San Jose State University, San José, CA 95192-0106, USA
178 Universidad Sergio Arboleda, 11022 Bogotá, Colombia
179 University of Sheffield, Sheffield S3 7RH, UK
180 SLAC National Accelerator Laboratory, Menlo Park, CA 94025, USA
181 University of South Carolina, Columbia, SC 29208, USA
182 South Dakota School of Mines and Technology, Rapid City, SD 57701, USA
183 South Dakota State University, Brookings, SD 57007, USA
184 Southern Methodist University, Dallas, TX 75275, USA
185 Stony Brook University, SUNY, Stony Brook, NY 11794, USA
186 Sun Yat-Sen University, Guangzhou 510275, China
187 Sanford Underground Research Facility, Lead, SD 57754, USA
188 University of Sussex, Brighton BN1 9RH, UK
189 Syracuse University, Syracuse, NY 13244, USA
190 Universidade Tecnológica Federal do Paraná, Curitiba, Brazil
191 Texas A&M University, College Station 77840, USA
192 Texas A&M University-Corpus Christi, Corpus Christi, TX 78412, USA
193 University of Texas at Arlington, Arlington, TX 76019, USA
194 University of Texas at Austin, Austin, TX 78712, USA
195 University of Toronto, Toronto, ON M5S 1A1, Canada
196 Tufts University, Medford, MA 02155, USA
197 Universidade Federal de São Paulo, São Paulo 09913-030, Brazil
198 Ulsan National Institute of Science and Technology, Ulsan 689-798, South Korea
199 University College London, London WC1E 6BT, UK
200 Valley City State University, Valley City, ND 58072, USA
201 Variable Energy Cyclotron Centre, Kolkata, West Bengal 700 064, India
202 Virginia Tech, Blacksburg, VA 24060, USA
203 University of Warsaw, 02-093 Warsaw, Poland
204 University of Warwick, Coventry CV4 7AL, UK
205 Wellesley College, Wellesley, MA 02481, USA
206 Wichita State University, Wichita, KS 67260, USA
207 College of William and Mary, Williamsburg, VA 23187, USA
208 University of Wisconsin Madison, Madison, WI 53706, USA
209 Yale University, New Haven, CT 06520, USA
210 Yerevan Institute for Theoretical Physics and Modeling, Yerevan 0036, Armenia
211 York University, Toronto M3J 1P3, Canada

Received: 31 March 2022 / Accepted: 24 June 2022

© The Author(s) 2022

Abstract DUNE is a dual-site experiment for long-baseline neutrino oscillation studies, neutrino astrophysics and nucleon decay searches. ProtoDUNE Dual Phase (DP) is a $6 \times 6 \times 6 \text{ m}^3$ liquid argon time-projection-chamber (LArTPC) that recorded cosmic-muon data at the CERN Neutrino Platform in 2019–2020 as a prototype of the DUNE Far Detector. Charged particles propagating through the LArTPC produce ionization and scintillation light. The scintillation light signal in these detectors can provide the trigger for non-beam events. In addition, it adds precise timing capabilities and

improves the calorimetry measurements. In ProtoDUNE-DP, scintillation and electroluminescence light produced by cosmic muons in the LArTPC is collected by photomultiplier tubes placed up to 7 m away from the ionizing track. In this paper, the ProtoDUNE-DP photon detection system performance is evaluated with a particular focus on the different wavelength shifters, such as PEN and TPB, and the use of Xe-doped LAr, considering its future use in giant LArTPCs. The scintillation light production and propagation processes are analyzed and a comparison of simulation to data is performed, improving understanding of the liquid argon properties.

^ae-mail: clara.cuesta@ciemat.es (corresponding author)

1 Introduction

The Deep Underground Neutrino Experiment (DUNE) [1] aims to address key questions in neutrino physics such as measuring the CP violating phase and the neutrino mass ordering with an intense muon neutrino beam produced at Fermilab [2]. The physics program also addresses non-beam physics such as nucleon decay and beyond the Standard Model searches [3] and the detection and measurement of the electron neutrino flux from a potential core-collapse supernova within our galaxy [4]. DUNE will consist of a near detector placed at Fermilab close to the production point of the neutrino beam of the Long-Baseline Neutrino Facility (LBNF) to measure the unoscillated neutrino interaction rate, and four 17-kt liquid-argon time-projection chambers (LArTPCs) as far detector in the Sanford Underground Research Facility (SURF) at 4300 m.w.e. depth at 1300 km from Fermilab [5,6] where the neutrino interaction will be measured after neutrinos have oscillated.

The ProtoDUNE Dual Phase (DP) detector [7,8] was operated from 2019 to 2020 at the CERN Neutrino Platform to demonstrate the LArTPC DP technology at large scale as a prototype for one of the DUNE far detector modules. ProtoDUNE-DP has an active volume of $6 \times 6 \times 6 \text{ m}^3$ corresponding to an active mass of 300 t (total LAr mass of 750 t), being the largest DP LArTPC ever operated. In ProtoDUNE-DP the electric drift field is oriented in the vertical direction, causing the electrons to drift vertically towards the anode at the top. The ionization charge is then extracted, amplified, and detected in gaseous argon above the liquid surface by the charge readout planes (CRPs). The DP technology allows a good signal to noise ratio (> 10 for 6-m drift at 500 V/cm drift field) and a fine spatial resolu-

tion ($\sim 3.125 \times 3.125 \times 0.64 \text{ mm}^3$) [9] enabling the construction of large active volumes making efficient use of the LAr volume. The CRP consists of the extraction grid which bounds the active volume, large electron multipliers (LEMs) to produce the charge avalanche, and the anode to collect the electrons. In ProtoDUNE-DP, two fully instrumented CRPs of $3 \times 3 \text{ m}^2$, and two CRPs without LEMs are installed. The scintillation light signal is collected by a photon detection system (PDS) constructed out of photo-multiplier tubes (PMTs). The PDS goals are to provide a trigger and to determine precisely the event time, with capability to perform calorimetric measurements and particle identification. Two Cosmic Ray Tagger (CRT) panels with eight scintillator bars ($1.44 \text{ m} \times 0.12 \text{ m}$) per panel are placed on opposite sides of the ProtoDUNE-DP cryostat to trigger on muon-tracks passing through both CRTs. Figure 1 shows a diagram of ProtoDUNE-DP with the layout and dimensions of the CRPs, PMTs and CRTs. The PDS layout is optimized to maximize the collected light [10].

As charged particles pass through LAr, they create pairs of positively charged argon ions (Ar^+) and free electrons and also produce excited atoms (Ar^*). When ionized and excited argon atoms couple to neutral Ar atoms, they produce the molecular states Ar_2^+ and Ar_2^* , respectively. The first one eventually recombines with an electron producing Ar_2^* . In both processes (recombination and excitation) the decay of the final state results in the emission of a vacuum ultraviolet (VUV) photon within a wavelength centered at $127 \pm 8 \text{ nm}$ [11] constituting the primary scintillation light (S1) signal:

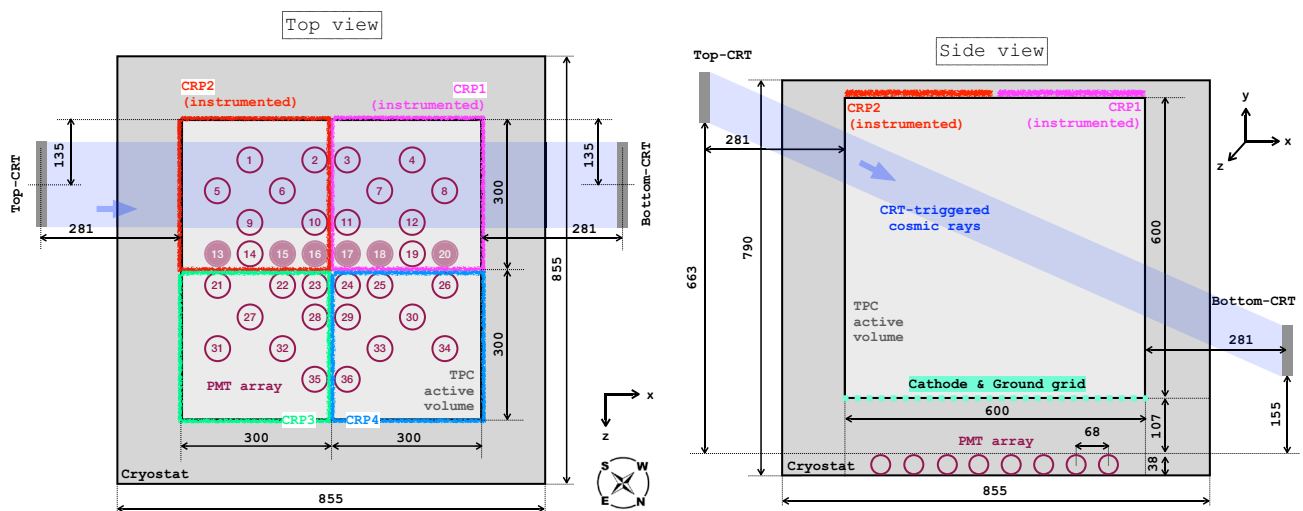
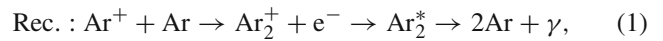


Fig. 1 Views of ProtoDUNE-DP. Dimensions and positions of the major elements are indicated (in units of centimeters). The drift direction corresponds to the y-axis. The PMTs are represented with circles and, in the top view, the empty circles correspond to PEN PMTs and the filled circles to TPB PMTs

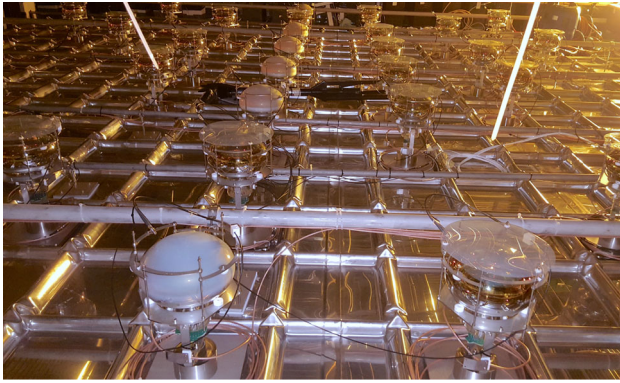


Fig. 2 ProtoDUNE-DP PDS formed of 36 PMTs installed at the bottom of the cryostat at CERN. The front left PMT has TPB coating and the front right PMT has PEN sheet

In order for the recombination process to occur, an electron cloud surrounding the Ar_2^+ is needed. Hence the scintillation light yield depends on the electric field. Ar_2^* has two possible states, a singlet and a triplet state. The singlet transition to the ground state Ar_2 has a short decay time $\tau_{\text{fast}} \sim 6$ ns, while the triplet transition to the same ground state is allowed only because of spin-orbit coupling and has a much longer lifetime $\tau_{\text{slow}} \sim 1.6 \mu\text{s}$ [12].

In addition, electroluminescence secondary scintillation light, called S2, is produced in the gas phase of the dual phase LArTPC when electrons, extracted from the liquid, are accelerated in the electric field of the LEMs. The S2 signal also has 127 nm wavelength. The time difference between the S1 and the S2 signals reflects the drift time of the original ionization in the liquid phase up to the gas phase, and the S2 duration, which can be up to hundreds of microseconds, is directly related to the track topology and covers the span of the electron drift time.

The PDS of ProtoDUNE-DP [13] is formed of 36 8-in. cryogenic R5912-02MOD PMTs from Hamamatsu [14, 15], placed below the cathode grid. As the PMTs are not sensitive to VUV light, a wavelength shifter converts 127-nm photons into visible photons. Two different wavelength shifters were deployed. A sheet of polyethylene naphthalate (PEN) is placed on top of 30 PMTs and the other 6 PMTs have tetraphenyl butadiene (TPB) directly coated on them. Figure 2 shows a picture of the PDS installed in ProtoDUNE-DP.

A light calibration system (LCS) was developed for ProtoDUNE-DP to monitor the PMT performance and obtain an equalized PMT response [16]. The light source consists of 6 blue LEDs and a silicon photo-multiplier (SiPM) as reference sensor. The LEDs use a Kapustinsky [17] circuit as LED driver, and have a wavelength of 465 nm that matches the PMT maximum quantum efficiency. The calibration light is transmitted through a fiber system with a fiber-end pointing at each PMT photocathode.

This paper describes the ProtoDUNE-DP PDS performance after 18 months of operation considering its future use in giant LArTPCs with a particular focus on the wavelength shifting techniques. A study of the LAr scintillation and electroluminescence light production and propagation over large distances is presented. In Sect. 2, the ProtoDUNE-DP operation and collected light data are described. Section 3 details the performance of ProtoDUNE-DP PDS. In Sect. 4 the light simulation tools are detailed. The analyses of scintillation light propagation and production are discussed in Sect. 5 and the cosmic muon rate measured in ProtoDUNE-DP is described in Sect. 6. Studies using the electroluminescence light signal are summarized in Sect. 7. Finally the performance of the system using Xe-doped LAr is reviewed in Sect. 8.

2 ProtoDUNE-DP PDS operation at CERN

ProtoDUNE-DP collected cosmic-ray data from June 2019 until November 2020, operating with pure LAr and Xe-doped LAr in different conditions of electric fields. Muons are the most abundant charged particles in cosmic rays at surface, together with protons ($\sim 1\%$), and electrons and positrons ($\sim 0.1\%$). No beam data were taken with ProtoDUNE-DP.

The ProtoDUNE-DP operation faced issues that impacted the electric field conditions. A short circuit between the high-voltage (HV) source and a field-cage ring at approximately 1/3 the field-cage depth prevented reaching the nominal cathode voltage (-300 kV). The cathode HV was set at -50 kV and the drift field in the operation conditions was fairly uniform in the top part of the drift and away from the field cage walls. A COMSOL [18] simulation of the resulting drift field is shown in Fig. 3. Additionally, CRP operation was not straightforward due to the presence of bubbles on the LAr surface causing LEM and grid discharges. Given these limitations, data taken with the CRPs in combination with the PDS were very limited and the data presented in this paper were taken with the PDS alone. The operation conditions of ProtoDUNE-DP were 88 K with a thermal gradient present in the detector less than 20 mK and 1045 mbar.

The PDS started its operation as soon as the detector was purged with argon gas in June 2019. ProtoDUNE-DP operated fully filled with LAr from August 2019 until May 2020. In June 2020, an intervention on the HV extender was carried out with the aim of fixing the short circuit although the issue was not solved. In July 2020, the detector was re-filled using ~ 230 ton of Xe-doped LAr from ProtoDUNE-SP [19] contaminated with N_2 . In August 2020, operations were resumed and two additional N_2 injections took place to measure the effect of N_2 contamination in the light attenuation length. Table 1 summarizes the different doping concentrations in ProtoDUNE-DP.

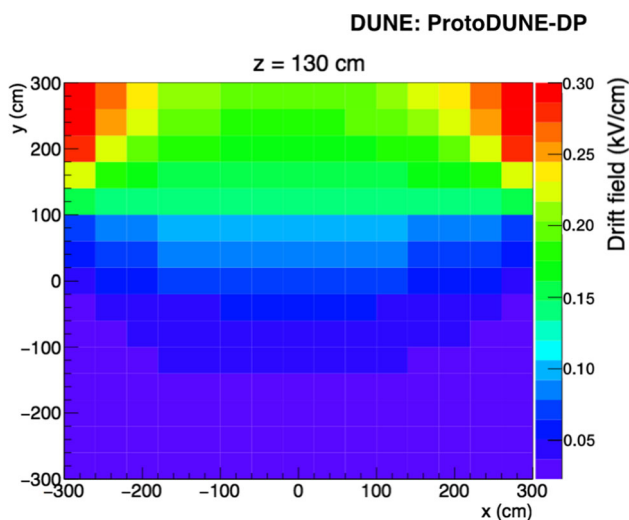


Fig. 3 Map of the drift field in ProtoDUNE-DP with cathode at -50 kV simulated using COMSOL. A particular plane of the active volume is shown (vertical plane at 130 cm from a field cage wall). The drift direction is along the y -axis and the color scale represents the electric field strength. The discontinuity at $y \sim 100$ cm is due to the HV failure described in the text

Table 1 Summary of Xe and N_2 doping concentrations in ProtoDUNE-DP. Units are ppm in mass for Xe, and ppm in volume for N_2

Situation	[Xe] (ppmm)	[N_2] (ppmv)
LAr + Xe + N_2	5.8	2.4
1st N_2 injection	5.8	3.4
2nd N_2 injection	5.8	5.3

The PDS took data on a daily basis during short time periods (typically 1–2 h/day). PMT HVs had to be switched off during the operation of some monitoring systems that emit light, like the purity monitors or the cryogenic cameras, to avoid any damage to the PMTs. Especially at the beginning of the data taking period, this happened very often to survey the status of the liquid surface and charge readout planes. Longer time periods of PDS data taking (~ 12 h) were allowed, typically at night, proving the stability of the PDS.

A dedicated light data acquisition and calibration software was developed for ProtoDUNE-DP [20]. The software allows the user to choose the acquisition trigger mode, control and define the acquisition settings (front-end and high-voltage), and provides the graphical user interface. The light readout front-end electronics is based on the commercial ADC V1740 from CAEN [21]. This 12-bit VME digitizer has 64 analog input channels with 2 V_{pp} dynamic range and a maximum sampling rate of 62.5 MS/s. All data presented in this paper were taken with 16-ns sampling, and different time acquisition windows depending on the configuration (from 2μ s to 4 ms).

Individual PMT waveforms were recorded for analysis, so each event contains 36 waveforms. An example of a PMT self-trigger event is shown in Fig. 4 and an individual PMT waveform is shown in Fig. 5. In the off-line analysis, various properties of the waveform are evaluated: the integrated charge in a given time period (in photo-electron units, PE), the time when the waveform reaches the minimum value (t_0), the amplitude of the event, and the baseline mean and standard deviation (STD).

The PDS system took data in three trigger modes:

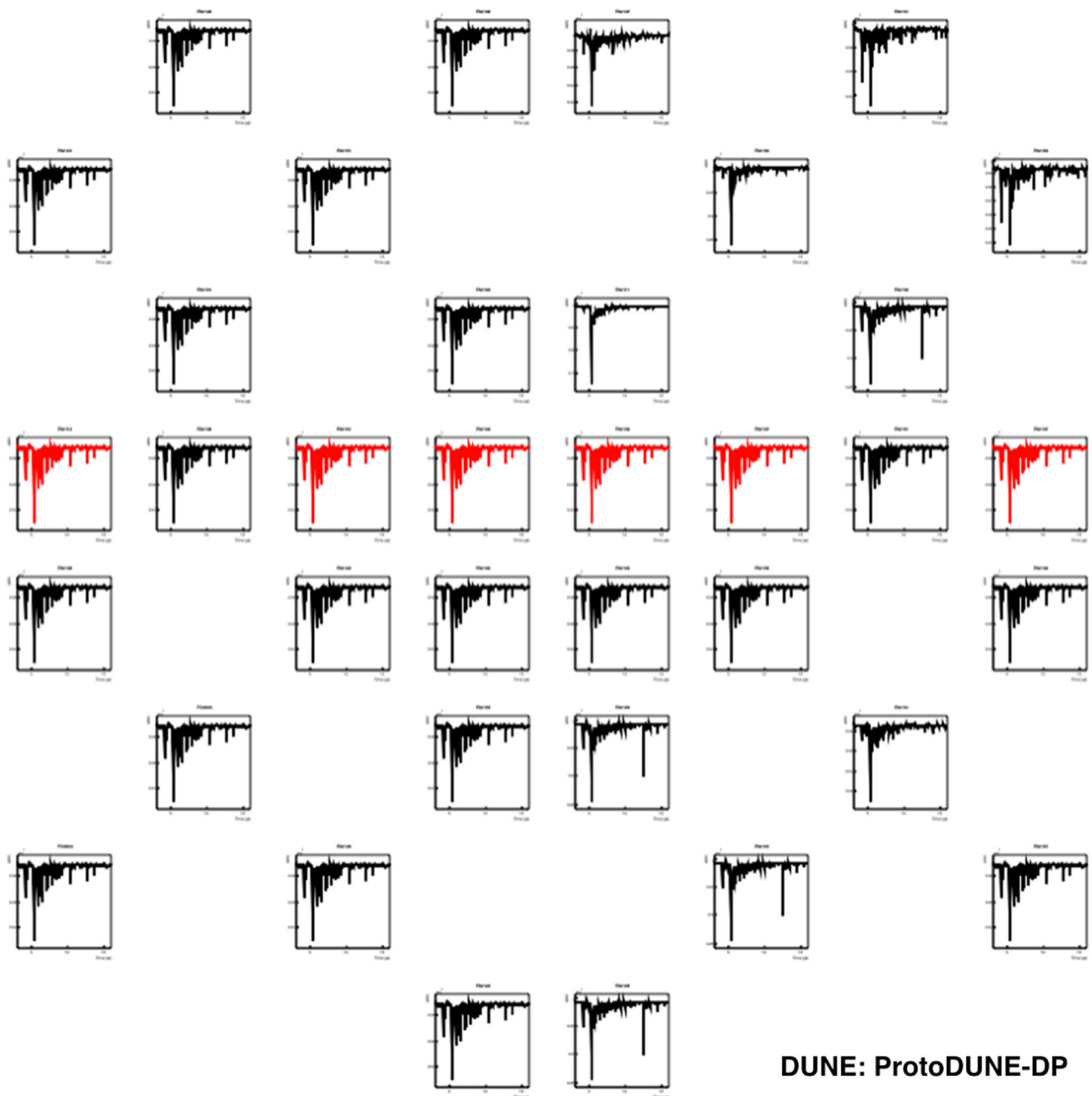
- PMT self-trigger: Provided by the PDS when a set number of PMT signals (or more) over a given threshold are in coincidence. The trigger rate is in the Hz–kHz range depending on the customizable threshold and the number of PMTs required to pass the threshold. In this trigger mode, not only single tracks are collected, but also showers and multi-track.
- CRT trigger: In this case the PDS receives an external trigger signal from the CRT planes at an average rate of 0.3 Hz. The CRT trigger mode allows the recording of single tracks with known topology.
- Calibration mode: An external trigger signal is received from the light calibration system at 1 kHz synchronized with the calibration light pulse sent to the PMTs. This mode also allows taking data with random trigger at a configurable rate turning off the LEDs.

A total of 130.7 million events were acquired during a live time of 675 h. Table 2 shows the summary of the data taken for the different trigger configurations. As shown in Table 3, most of the light data were acquired without electric drift field, and therefore contain only primary scintillation signals. Events with secondary light signals were collected for different drift and amplification field conditions. An important sample of events was recorded during the commissioning phase of the system with varying conditions (test mode).

3 ProtoDUNE-DP PDS performance

All 36 PMTs were operational throughout of data taking, allowing the validation of the basic performance of the PDS. A coincident primary scintillation light signal (S1) detected by all 36 PMTs is visible in Fig. 4. The time alignment among PMT signals has been measured for all channels to be better than 16 ns.

The low noise in the baseline of the signals is notable, as the baseline presents very small fluctuation: 0.6 ± 0.1 ADC (0.29 ± 0.05 mV). The error includes the differences among PMTs and the stability along the time. In addition, the baseline stability with time is shown in Fig. 6.



DUNE: ProtoDUNE-DP

Fig. 4 Example of a PMT self-trigger event showing the waveforms corresponding to the 36 PMTs according to their relative position in the detector. The PEN PMTs are shown in black and TPB PMTs in red.

The x -axis range is $0\text{--}16\ \mu\text{s}$ for all PMTs while the y -axis range (in ADC counts) varies for each PMT and is optimized to best display the S1 signal

With the aim of understanding the performance of the PDS, the gain calibration results are shown in Sect. 3.1, the single photo-electron (SPE) is characterized in terms of amplitude and rate in Sect. 3.2, the relative performance of PEN and TPB is evaluated in Sect. 3.3, and the scintillation time profile is studied in Sect. 3.4.

3.1 Calibration

The main goal of the LCS is to calibrate the PMT response by determining the PMT gain during the operation of the detector. It is important to guarantee equalized PMT response and to measure the light collected in PE units. An accurate measurement of the collected light is essential for calorimetry

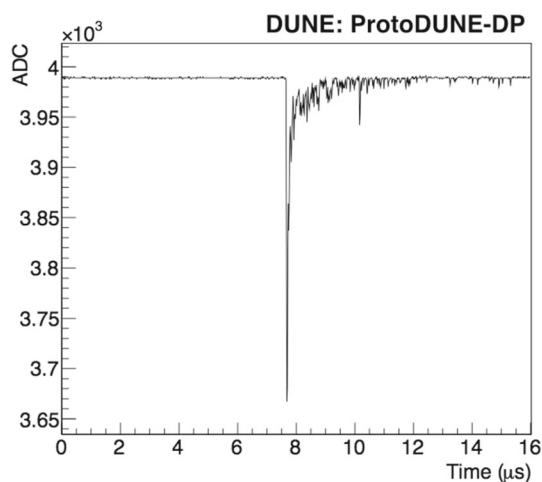


Fig. 5 Example of a scintillation light event in a ProtoDUNE-DP PMT at a gain of 10^7 in LAr without electric field

Table 2 Summary of trigger conditions indicating the number of events and total time of data taken in the different trigger configurations

Trigger	# of events (M)	Time (h)
PMT	85.3	96
CRT panels	0.6	515
Calibration	30	42
Random	14.7	21
Total	130.7	675

Table 3 Summary of the detector configurations indicating the number of events and total time of data taken with different voltage across LEMs

Drift field	LEM voltage	# of events (M)	Time (h)
OFF	–	85.1	342
ON	0kV	13.6	72
	2.5–3.6kV	7.7	212
Test	–	23.2	48
Total	–	130.7	675

and to estimate the detection efficiency of the PDS. The PMTs are typically operated at a gain in the range from $1 \cdot 10^7$ to $5 \cdot 10^7$ as a compromise between maximizing the sensitivity to the SPE and minimizing ADC-saturated events. The LCS illuminates the PMT photocathode at the SPE level in order to determine the PMT gain. The calibration light rate is kept to \sim kHz to avoid PMT fatigue [16].

The gain calibration method, based on measuring the SPE charge at a given voltage, is described in [16]. During operation, PMTs were biased at the HV required to achieve the target gain according to the calibration results. Calibrations were carried out weekly and a gain correction based on the closest calibration in time is applied in the analysis.

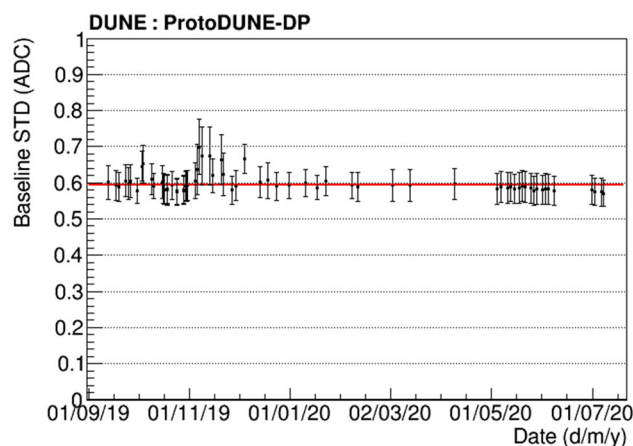


Fig. 6 Baseline mean STD during ProtoDUNE-DP operation. A fit to the mean value (0.6 ± 0.1 ADC) is shown in red and error bars represent the differences among the different PMTs

The calibrations performed during the detector operation allow to monitor the PMT gain stability with time. Figure 7 presents the gain evolution of all the PMTs during one year of regular operation of the LCS. It should be noted that the PMTs were switched on and off every day (sometimes several times on the same day). Despite this, it can be seen that the PMT gains are quite stable with time. In particular, the average value of the gain STD at 1500 V for 36 PMTs is 9%.

3.2 Single photo-electron characterization

The capability of measuring low energy signals depends on the signal-to-noise ratio and on the SPE rate from various background sources.

The SPE amplitude is characterized as a function of the PMT gain using calibration data. The SPE amplitude spectra are fitted with a Gaussian function for each PMT in order to obtain the mean amplitude (μ) and its corresponding standard deviation (σ) as functions of the PMT gain. The correlation between mean amplitude and gain is shown in Fig. 8, which allows the average SPE amplitude at any gain to be extracted. For instance, at a gain of 10^7 , the SPE amplitude is 7 ADC counts, implying a signal-to-noise ratio greater than 11 thanks to the small fluctuation of the baseline in the PMT waveforms, while σ is 2 ADC counts. An example of a SPE pulse in a PMT waveform at a gain of 10^7 is shown in Fig. 9. The SPE pulses have a full width at half maximum (FWHM) of 1 time sample (59%, 16 ns) or 2 time samples (40%, 32 ns).

The SPE rate is computed by counting the SPE pulses in the data samples taken with the random trigger. Pulses with an amplitude within the expected range ($\mu \pm 2\sigma$) are considered, ignoring the parts of the waveform affected by S1 signals larger than 1 PE. Without drift field, a SPE rate of

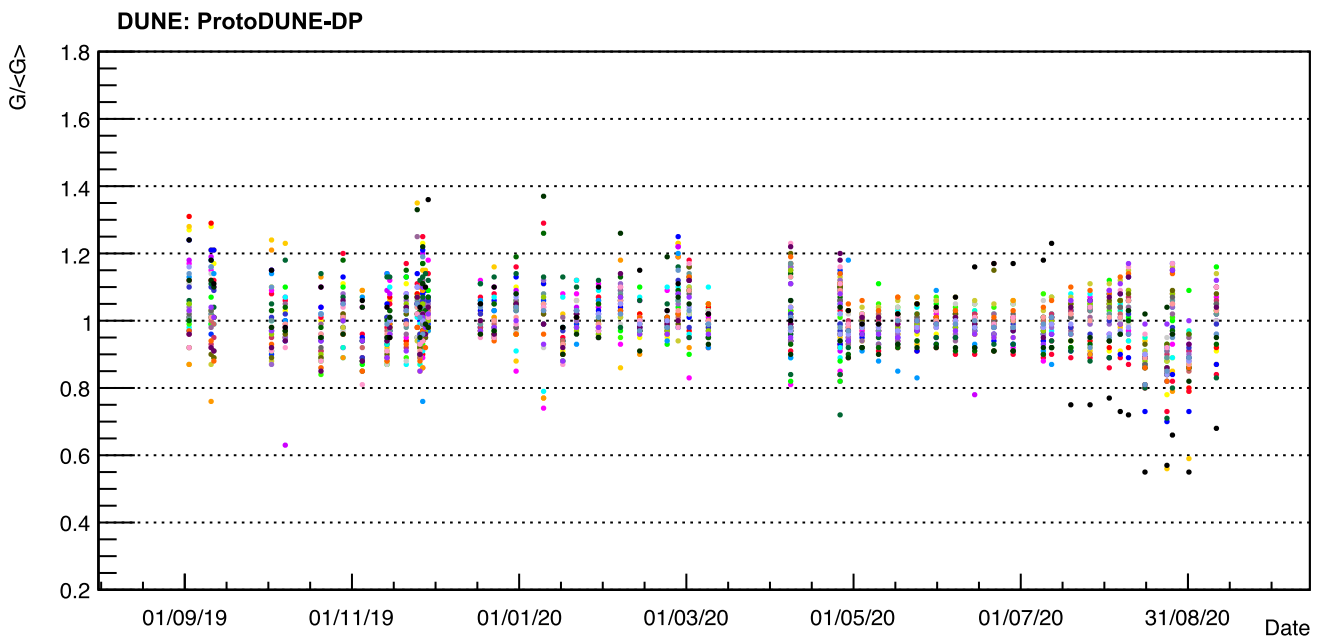


Fig. 7 Gain (G) stability with time for the 36 PMTs (one color per PMT) evaluated at 1500 V represented with respect to the average gain $\langle G \rangle$

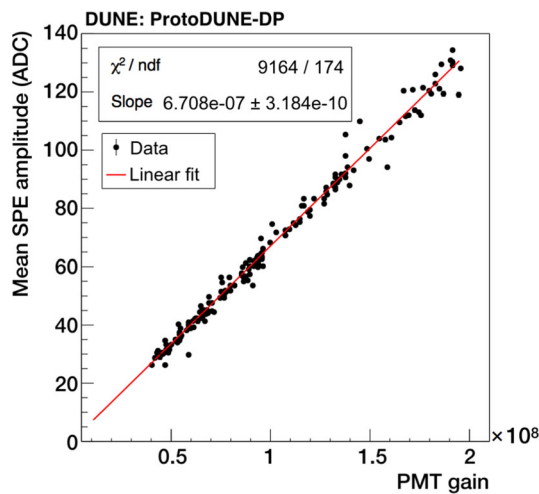


Fig. 8 Mean SPE amplitude from Gaussian fits as a function of the PMT gain, and linear fit. All PMTs are included but only data corresponding to gains that allow a proper fit are considered

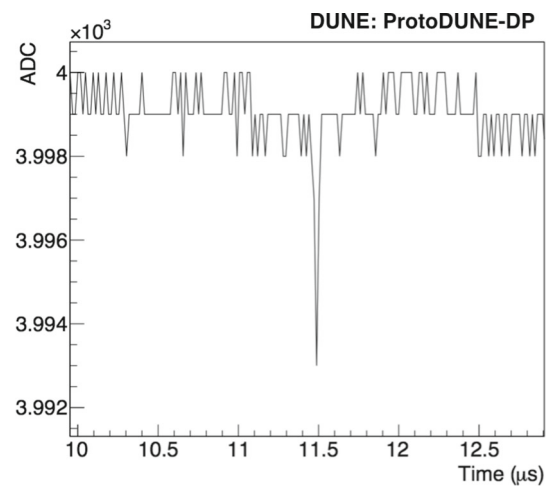


Fig. 9 Example of SPE pulse in a PMT waveform (10^7 gain)

~ 350 kHz is obtained for TPB PMTs, whereas PEN PMTs are less sensitive and a rate of ~ 170 kHz is measured.

There are several light contributions at the SPE level to the low-energy background detected by the PMTs. First, according to data analysis, cosmic muons are expected to be detected as SPE at ~ 35 kHz. Second, according to a dedicated simulation, natural radioactivity, mainly from 1.01 Bq/kg ^{39}Ar [22], 115 mBq/kg ^{85}Kr [22] and 0.09 mBq/kg ^{42}Ar [23], is expected to contribute with ~ 20 kHz. Lastly, it is known that the PMT dark current contributes with a SPE rate of ~ 1.7 kHz [14]. However, the measured rate is higher than the

expectation from these sources. A study [24] suggests that Ar_2^+ drifting to the cathode could explain the high SPE rate recently measured in several experiments as these molecules recombine with electrons and neutralize with electronegative impurities producing photons. Unfortunately, this hypothesis cannot be tested in our detector because of the non-uniform drift field.

3.3 Wavelength-shifting materials: PEN and TPB

The LAr scintillation light is produced at 127 nm, a wavelength which most photosensors are not sensitive to, and fluorescent materials are introduced to shift the photon wave-

length towards the visible range. ProtoDUNE-DP uses PMTs either covered with polyethylene naphthalate (PEN) foils or directly coated with tetraphenyl butadiene (TPB). While TPB is broadly used, PEN is a novel material, never used before in such a large scale experiment and whose efficiency is not well known. As TPB needs complex coating setups [25], the potential benefit of PEN comes from its simple handling, because PEN foils are flexible plastic sheets easy to fabricate and install. The PEN sample used in ProtoDUNE-DP is transparent and biaxially oriented, manufactured by GoodFellow [26]. It has been installed as round disks of 240 mm diameter and 0.125 mm thickness placed over the top of the PMT glass surface, as shown in Fig. 2. TPB was deposited over the PMT polished surface, using a dedicated evaporation system developed by the ICARUS experiment [25]. The coating density is 0.2 mg/cm², which corresponds to a coating thickness around 0.2 μm. Both PEN and TPB have a maximum of re-emitted photons around a wavelength of 430 nm [27, 28].

Photons produced after cosmic particles interact with the LAr will arrive at the wavelength-shifter (either PEN or TPB) and will convert into visible light that can be detected by the PMTs. The relative photon detection efficiency of the PEN-foil PMTs versus the TPB-coated PMTs, NPE_{PEN}/NPE_{TPB} , is experimentally determined by comparing the amount of light (in PEs) detected by a pair of PEN-TPB PMTs placed symmetrically with respect to the detector and the light source. An homogeneous response for the whole photocathode is considered.

Dedicated data-sets were taken selecting events with a signal amplitude larger than 13 PEs in the trigger PMT, a TPB-coated PMT placed at the center of the detector (channel 16 in Fig. 1). The PMT pairs are selected among PMTs symmetrically placed near the trigger PMT (for example, channels 17 and 23). As the event position is not known, the number of photons reaching the PMTs cannot be compared on an event by event basis, but it can be assumed that the amount of photons reaching both PMTs is on average the same. The cosmic-muon flux is assumed to be isotropic.

The response of five PMT pairs is compared at different gains (10^7 , $2 \cdot 10^7$, $5 \cdot 10^7$ and 10^8). The trigger configuration was kept constant in all data-sets, with the same gain ($5 \cdot 10^6$) and threshold (13 PEs in amplitude) in the trigger PMT in order to study the same event sample at different gains. To avoid saturation of the ADC and guarantee linear response of the PMTs, events with a signal amplitude larger than ~ 30 PEs on the trigger PMT are not included. This selection reduces the fraction of saturating events below 1% in all PMTs in all data-sets.

The average light collected on the PMTs for the selected events is ~ 200 PEs on TPB-coated PMTs, and ~ 50 PEs on PEN-foil PMTs. The NPE_{PEN}/NPE_{TPB} ratio is stable for each pair at different gains and different ranges. An average NPE_{PEN}/NPE_{TPB} ratio of 0.25 ± 0.03 is obtained, as

Table 4 First row: Value of the relative photon detection efficiency, NPE_{PEN}/NPE_{TPB} . The error represents the STD for all the PMT pairs. Second row: relative WLS efficiency of PEN and TPB, $\epsilon_{PEN}/\epsilon_{TPB}$

Parameter	Value
NPE_{PEN}/NPE_{TPB}	0.25 ± 0.03
$\epsilon_{PEN}/\epsilon_{TPB}$	0.35 ± 0.09

reported in Table 4. The error is the STD among PMT-pairs, which agrees with the expected error (0.03) due to the QE variation between 3 PMTs measured by the manufacturer. On average, ProtoDUNE-DP TPB-coated PMTs detect four times more photons than PEN-foil PMTs. This ratio is computed for a particular sample of muons; selecting events with a different track topology would vary this ratio.

Additionally, a simple model is proposed to compute the relative WLS efficiency of the two materials. The number of detected photoelectrons is given by:

$$NPE = \gamma \cdot \epsilon \cdot \Delta \cdot QE, \quad (3)$$

where γ is the number of VUV photons arriving to the wavelength shifter, ϵ is the WLS efficiency, Δ is the photon transport losses from the WLS to the PMT, and QE is the PMT quantum efficiency. Then, the relative conversion efficiency can be derived:

$$\frac{\epsilon_{PEN}}{\epsilon_{TPB}} = \frac{NPE_{PEN}}{NPE_{TPB}} \cdot \frac{\gamma_{coat}}{\gamma_{foil}} \cdot \frac{\Delta_{coat}}{\Delta_{foil}}. \quad (4)$$

The ratio of photons arriving to the TPB coating over the PEN foil is, on average, $\gamma_{coat}/\gamma_{foil} = 0.69 \pm 0.16$, as calculated using the cosmic-muon simulation described in Sect. 4. This factor depends on the selected sample, and the simulation of a different event topology would vary its value. The fact that the PEN foil receives 30% more photons than the TPB coating can be explained as its two faces are exposed to LAr while the TPB only has one.

Considering an isotropic re-emission of the TPB coating, only 50% of the photons will reach the photocathode ($\Delta_{coat} = 0.5$). For the PEN foil, the transport losses are simulated considering an isotropic re-emission in the foil, and it is found that $\Delta_{foil} = 0.247$, meaning that only 25% of the re-emitted photons will reach the photocathode due to the geometrical configuration of the foil with respect to the photocathode.

As a result, considering the geometrical differences and the measured ratio NPE_{PEN}/NPE_{TPB} , the relative WLS efficiency of both materials is estimated to be $\epsilon_{PEN}/\epsilon_{TPB} = 0.35 \pm 0.09$, as shown in Table 4. TPB produces three times more visible photons than PEN, for the same amount of incident VUV photons. This agrees with the value of 0.34 ± 0.01 reported in [29] for the same PEN sample.

To introduce the PMT response in the simulation, the effective PMT photon-detection efficiencies at 127 nm for

TPB-coated PMTs (E_{TPB}) and for PEN-foil PMTs (E_{PEN}) are estimated. This effective efficiency provides the amount of photoelectrons detected per incident VUV photon, and it can be calculated by:

$$E = \epsilon \cdot \Delta \cdot QE. \tag{5}$$

The PMT quantum efficiency (QE) was measured by the manufacturer for three of the PMTs at room temperature. They measured a value of $QE = 0.183 \pm 0.013$ at 430 nm, and it is assumed that the PMT QE is stable when going to cryogenic temperature [30,31]. Since the values of TPB efficiency at 127 nm reported in the literature show a large dispersion [32–34], a 100% TPB efficiency is assumed as in a previous work [35] ($\epsilon_{TPB}=1$). Then, assuming the PEN efficiency obtained by the relative performance of both systems in Table 4 ($\epsilon_{PEN} = 0.35 \pm 0.09$), the corresponding effective efficiency for TPB-coated and PEN-foil PMTs are $E_{TPB} = 0.09$ and $E_{PEN} = 0.016$, making the TPB coated-PMT six times more efficient. However, positioning the PEN foil directly over the PMT glass, as the TPB coating, would double its effective efficiency. These efficiencies are used in the analyses presented in Sects. 5 and 6.

3.4 LAr scintillation time profile

The scintillation light emission in LAr has a characteristic time dependence as mentioned in Sect. 1. To get the scintillation decay times from the PMT waveforms, signals from cosmic muons are selected by triggering on a TPB-coated PMT with a minimum amplitude of 25 PEs. The PMT gain is set at $5 \cdot 10^6$ to minimize the ADC saturation, and events saturating the PMT [36] are excluded. Eleven of the PMTs suffer this phenomenon more frequently and are excluded for this analysis.

An average time profile is generated for each PMT. The average waveform in the absence of drift field for one PMT is shown in Fig. 10. Waveforms are well described by Eq. (6):

$$f(t) = \sum_{j=fast,slow,int} \frac{2A_j}{\tau_j} \exp\left[\frac{\sigma^2}{2\tau_j^2} - \frac{t-t_0}{\tau_j}\right] \times \left(1 - \text{Erf}\left[\frac{\sigma^2 - \tau_j(t-t_0)}{\sqrt{2}\sigma\tau_j}\right]\right) \tag{6}$$

a sum of three exponential functions convoluted with a Gaussian function to represent the detector response. Although the scintillation time profile should in principle have only two components, from the decay to ground state of singlet (τ_{fast}) and triplet (τ_{slow}) argon excimers, an intermediate component (τ_{int}) is added in order to improve the fit as reported also by other LAr experiments [35]. Given the 16-ns digitization sampling, the fit has a limited sensitivity to τ_{fast} and this parameter is fixed to 6 ns [12]. Additionally, two signal

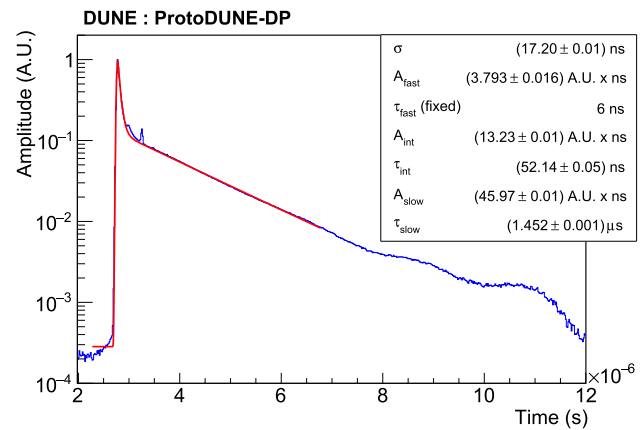


Fig. 10 Example of the average scintillation waveform of a PEN PMT (blue). The fit to Eq. 6 is shown in red. The corresponding parameters are shown in the legend

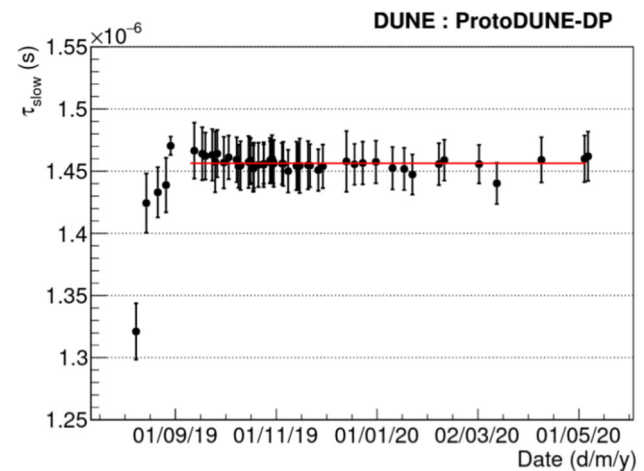


Fig. 11 Monitoring of the τ_{slow} component of the scintillation time profile during the detector operation. The error bars show the STD of the measurements for the different PMT waveforms. Red line at $\tau_{slow} = 1.46 \mu\text{s}$ shows the average from September 2019 when stable operation began

reflections at the flange feed-through appear ~ 200 ns and ~ 400 ns after the maximum, affecting the sensitivity to the τ_{int} measurement. To mitigate this, the bins containing the reflections are excluded from the fit.

Purity is critical in LArTPCs, since impurities can reduce the signal by trapping the ionization electrons. The purity can be monitored using the PDS by measuring the lifetime of the triplet molecular argon excimers, τ_{slow} . Figure 11 shows the evolution of the average τ_{slow} during the operation of ProtoDUNE-DP. The purity improved when the LAr purification system was turned on, and remained stable during the whole operation. The value of τ_{slow} is $1.46 \pm 0.02 \mu\text{s}$, with the error corresponding to the STD among the PMT waveforms. This average value has a small variation over time of just $0.004 \mu\text{s}$. The absolute value indicates a high LAr purity at the ppb level. No significant difference is observed

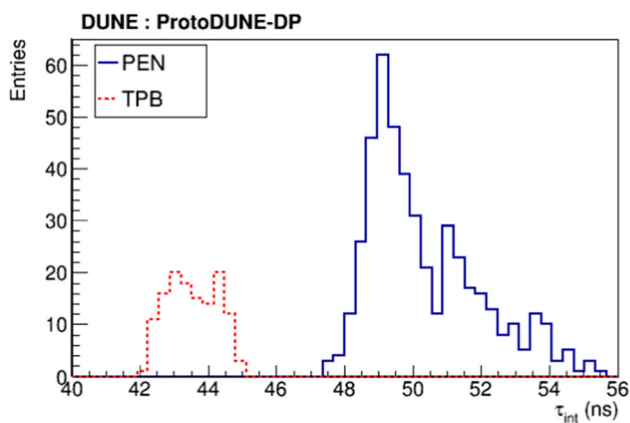


Fig. 12 τ_{int} distribution obtained from the fit to the average waveform for PEN (blue) and TPB PMTs (red)

in τ_{slow} between PEN and TPB PMTs. On average, τ_{slow} is $1.45 \pm 0.02 \mu\text{s}$ on PEN PMTs and $1.46 \pm 0.02 \mu\text{s}$ on TPB PMTs.

Figure 12 shows the value of τ_{int} for PEN and TPB PMTs obtained from the fit of the average waveforms using data sets for which the purity was already stable, from September 2019 to May 2020. An average value of $50.3 \pm 1.7 \text{ ns}$ is obtained for the PEN PMTs, and a faster response of $43.6 \pm 0.7 \text{ ns}$ for the TPB PMTs. The clear difference between the two different WLS points to a delayed emission time by the WLS material, as proposed in [37, 38].

4 Cosmic-muon light simulation

ProtoDUNE-DP light simulations are carried out using LArSoft [39], a physics software package designed for LAr neutrino experiments, such as DUNE.

The detailed geometry of the ProtoDUNE-DP detector has been implemented in Geant4 [40] using geometry description markup language (GDML) files. It includes the full cryostat with its support structure, cathode, field cage, LEMs, PMTs and ground grid.

The simulation of the cosmic-induced particles reaching ProtoDUNE-DP is based on CORSIKA (COsmic Ray Simulation for KAscade) [41], a Monte-Carlo (MC) simulation package. It is based on a multi-component model of primary cosmic rays, the constant mass composition (CMC) model [42], for a more complete modeling of the flux. CORSIKA generates showers from each specific cosmic ray type (Fe, He₂, Mg, proton) according to a power law distribution of the primary particle energy. The FLUKA model [43] describes the hadronic shower propagation. The LArSoft simulation draws from a random set of pre-generated air showers from a specific database created with CORSIKA. The number of showers per event and per primary particle source is extracted

according to a Poisson distribution around the predicted average number of primary cosmic rays for each source. The detector location (CERN), altitude and latitude, is used. The start time and spatial origin of the cascades of secondary particles are chosen randomly, and time and space correlations of the particles within each shower are preserved.

Muons crossing the CRT panels of ProtoDUNE-DP are also simulated. Single muons are generated with a defined initial position, momentum, and momentum spread. The energy distribution of the muons is taken from CORSIKA for a more realistic outcome. The data-driven track entry/exit distributions in the CRT panels are taken as inputs to define the track topology of the events. A topological selection is carried out and only muons with a complete trajectory between the CRTs are accepted, as deviations from the ideal straight trajectory can appear during the propagation through the detector and muons can decay along the track length.

The cosmic muons simulated with the event generators enter the LAr volume and deposit energy along their tracks as they interact with LAr. An incident muon behaves as a minimum ionizing particle (MIP) and deposits about 2 MeV/cm. First, the simulation of the muon energy deposition is performed in Geant4. Then, the number of scintillation photons is computed by multiplying the deposited energy by a light yield of $4 \cdot 10^4$ scintillation photons per MeV in the absence of a drift field. The time profile is simulated with an exponential fast decay of 6 ns for 30% of the photons, and an exponential slow decay of 1590 ns for the other 70% of the photons. Simulations were carried out before obtaining the ProtoDUNE-DP results described in Sect. 3 and no intermediate component is included. No drift field is assumed in this simulation to match the data taking conditions. Note also that only cosmic particles are simulated (only muons in the CRT case), and backgrounds from natural radioactivity are not currently included in the simulation.

The photon propagation in LAr, from the production point to the PMT array, is performed with Geant4 in LArSoft. The VUV-light attenuation due to absorption by impurities in LAr is simulated (20-m absorption length, equivalent to 3 ppmv of nitrogen contamination in LAr [44]) as well as the Rayleigh scattering length (RSL) (99.9 cm as baseline value [45], but also a shorter length of 61.0 cm [46] is tested). A VUV reflectance of 26% in aluminum is taken (field cage) [47], and the same VUV reflectance is assumed for stainless steel (SS) surfaces (cryostat walls, cathode and ground grid) [48]. Full absorption is considered for the rest of the materials. Table 5 summarizes the relevant parameters of the light propagation used in the simulation.

The complete simulation of the propagation of all the photons produced by each particle crossing the detector would require an enormous amount of CPU time. Hence, pre-generated libraries are employed to simulate the light propagation in an efficient way: a Geant4-driven simulation

Table 5 Parameters of the light propagation simulation in ProtoDUNE-DP

Parameter	Baseline value	Alternative
Absorption length	20 m	–
RSL	99.9 cm	61.0 cm
VUV reflectance	26% in Al & SS, 0% for the rest	0% for all
Voxel size	$0.34 \times 0.32 \times 0.34 \text{ m}^3$	–

is generated and the results are stored and parametrized in the so-called photon libraries. The LAr volume is divided into 3D voxels and 10^8 photons per voxel are isotropically and uniformly generated. A photon library contains, for each PMT-voxel combination: the visibility (photon detection probability), the minimum time for the light to reach the PMT (arrival time), and the Landau-fit parameters of the propagation time distribution. In order to mitigate the relatively large size of the voxels, 3D interpolations among them are used at each step of the track.

Three different photon libraries are generated to study the impact of several parameters in ProtoDUNE-DP: (A) the baseline photon library with 99.9-cm RSL and 26% VUV-light surface reflectance, (B) a library with 61-cm RSL and 26% of surface reflectance, and (C) a library with 99.9-cm RSL and no reflection. The maps with the detected light per deposited MeV across the volume for the baseline photon library (A) are displayed in Fig. 13.

The PMT response is simulated with a dedicated module that produces a waveform for each PMT. Each 127-nm photon arriving to the WLS has a probability to produce

a photoelectron in the PMT photocathode. The WLS-PMT photon-detection efficiency includes the WLS efficiency, the propagation of the visible light from the WLS towards the photocathode, and the PMT quantum efficiency. The values used in the light simulation are taken from studies presented in Sect. 3.3: $E_{\text{TPB}} = 0.09$ and $E_{\text{PEN}} = 0.016$.

Waveforms are produced by adding the SPE response for each detected photon. The simulated PMT response is linear, and includes a dark current component of 1.7 kHz [16]. The waveform digitization considers a 16-ns sampling matching the data acquisition system.

5 Light production and propagation in LAr measured with cosmic muon data

The pure LAr of ProtoDUNE-DP is an optimal medium to study the scintillation light production, propagation and collection in a LAr volume. The experiment provides valuable technical feedback for future light detection systems as well as results on the scintillation light mechanisms in LAr. In this section, PMT data acquired with the CRT-trigger system are analyzed to profit from the off-line reconstruction of the track trajectory that such a trigger allows. Muon tracks crossing the detector diagonally and in the downward direction are selected. Information about the distance the light travels from its production point in the LAr volume to the PMT detecting the signal is retrieved.

The analysis focuses on the 30 PEN PMTs because they allow exploring a wider track-PMT distance range than the TPB PMTs. Consistent results are obtained with the TPB PMTs. The S1 charge (number of PEs) of each triggered signal is obtained by integrating the PMT waveform in a

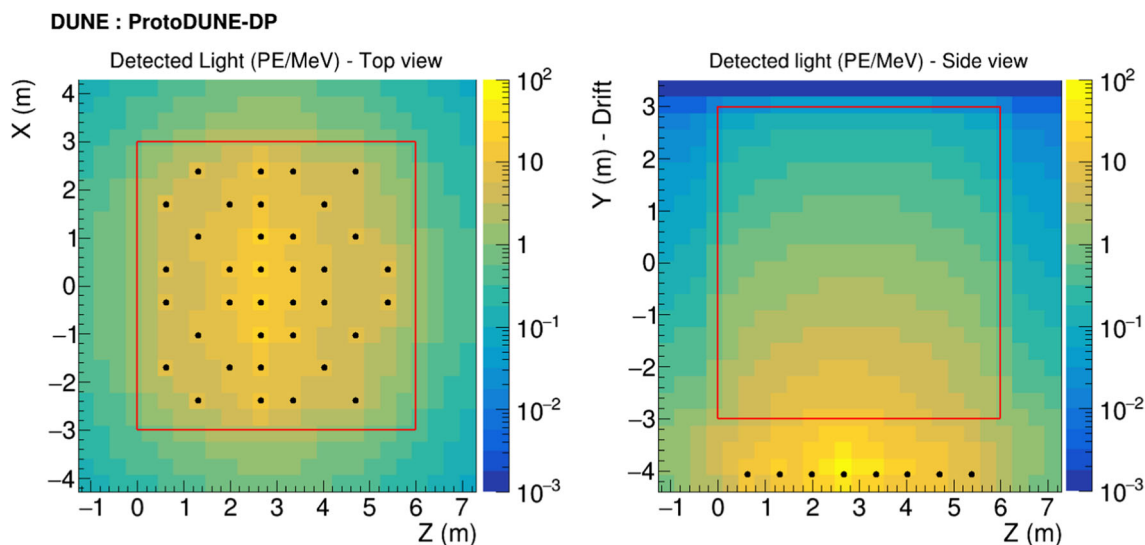


Fig. 13 Maps of the detected light (sum of PMT visibilities multiplied by efficiency, $E_{\text{TPB}} = 0.09$ and $E_{\text{PEN}} = 0.016$) per voxel for the baseline photon library in ProtoDUNE-DP: $4 \cdot 10^4$ photons per MeV, 99.9 cm

of RSL and 26% VUV reflections. The PMT positions are represented with black dots and the active volume with a red rectangle

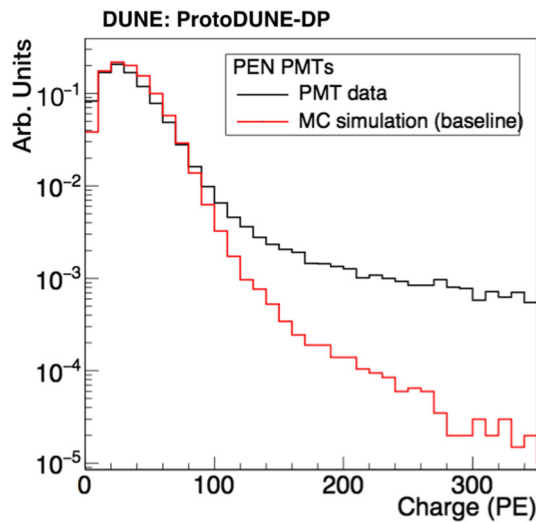


Fig. 14 Normalized distributions of the collected S1 charge for CRT triggered light data and simulation

4- μ s window. An event selection is made in both data and simulation to obtain comparable event samples:

1. Time of flight (data)/geometrical cut (MC): a data event is considered a good muon-candidate if the time of flight between the CRT panels (from top to bottom) is between 40 and 45 ns, and only one scintillating bar per panel is triggered. This cut contributes to the rejection of background events like electrons, particle showers, muon bundles and fake triggers. In the simulation case, only CRT-trigger-like muons are kept by requiring that the muon-track trajectory crosses both CRTs.
2. Stable baseline before trigger: this cut intends to avoid the pile-up of signals. The waveform RMS is obtained in a 1- μ s window before the signal trigger and the baseline is considered to be stable if the result is below 1 ADC count.
3. No ADC saturation: data events with waveforms saturating the ADC are excluded, both in data and MC.
4. Maximum charge: the charge per event must be below 100 PE for PEN PMTs. This limit is applied to suppress high-energy events (vertical showers instead of diagonal muons) that affect the distribution of interest in data but not in the MC as they are not simulated, see Fig. 14.

Since the propagation effects on the collected charge by the PMTs depend on their distance to the muon track, analyses shown in this section are mainly based on the correlation between the S1 signal (S1 charge in PE units) and the minimum distance from the muon track to the detecting PMT (simply referred to as track-PMT distance). Figure 15 shows the 2D distribution of these variables for data and MC. A good agreement is observed up to ~ 5 m; beyond that dis-

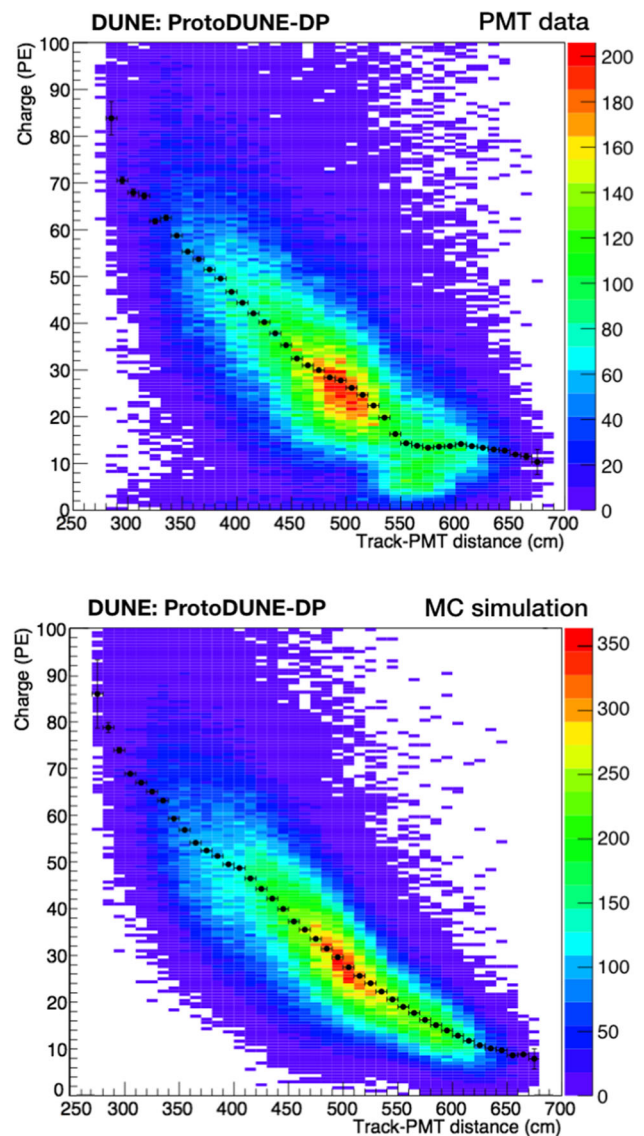


Fig. 15 Collected S1 charge versus track-PMT distance for PEN PMTs: Light data (top) and MC sample (bottom). The color maps contain all the S1 signals detected by the PMTs and passing the event selection. A Gaussian fit of each charge-distribution every 10 cm is performed and the mean values are plotted in black over the map. The vertical error bars correspond to errors from the fits and a 5-cm distance uncertainty (horizontal error bars) is included

tance, the correlation between charge and distance is lost in data, presumably, because low-energy background (only present in data and contributing with up to 8-9 PE per integration window) prevails over the signal. The profile histogram superimposed on the 2D plot corresponds to a Gaussian fit of the charge-distribution every 10 cm. In the case of the data samples, an additional systematic error of 4% (determined by varying the PMT gain) is added in quadrature to the fit error of the charge.

The top-view light detection maps (average S1 charge per optical channel) for the PEN PMTs both for data and MC are

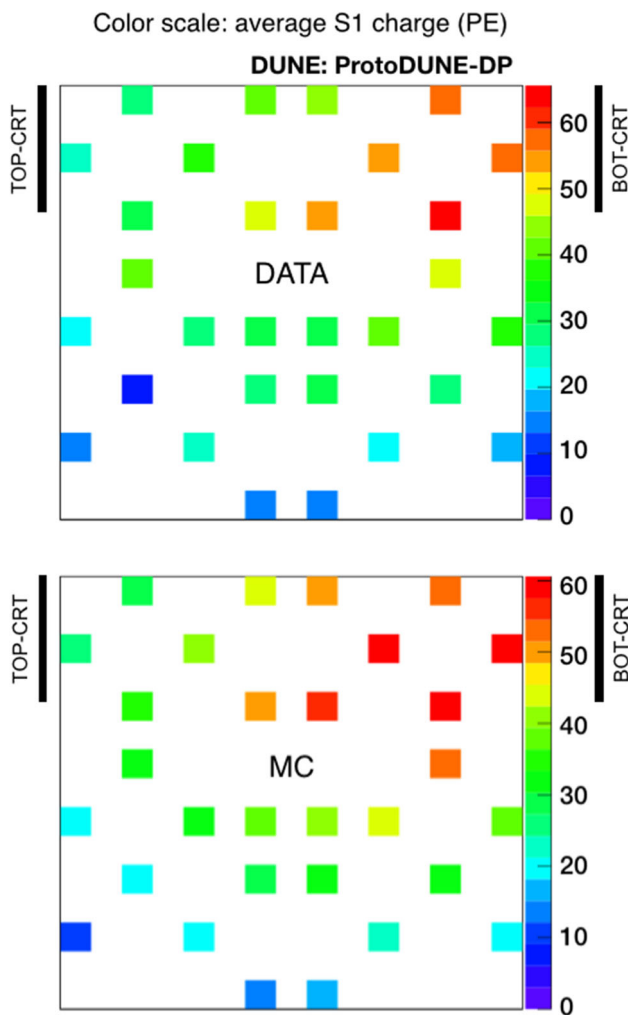


Fig. 16 Average S1 charge per channel (in PE) in CRT-trigger mode: top view of PEN-PMT array for data (top panel) and simulation (bottom panel). Each color square represents one PMT channel at its position in the detector. The approximate positions of the CRT frames are indicated with black lines

presented in Fig. 16. The obtained light detection patterns reproduce the expected gradient: the PMTs which are closer to the bottom CRT (top right corner in the top view) detect more light than the rest.

5.1 Drift field effect on light production

The reduction of the detected light with the increasing drift field is investigated. This reduction is due to the suppression of the electron-ion recombination by drift field, which reduces the primary scintillation light production. The electric field in ProtoDUNE-DP is not uniform across the active volume, which makes infeasible a complete understanding of the drift field effect over the light production. Nonetheless, the light levels detected with the PDS without drift field and at the maximum operating cathode HV (−50 kV) are com-

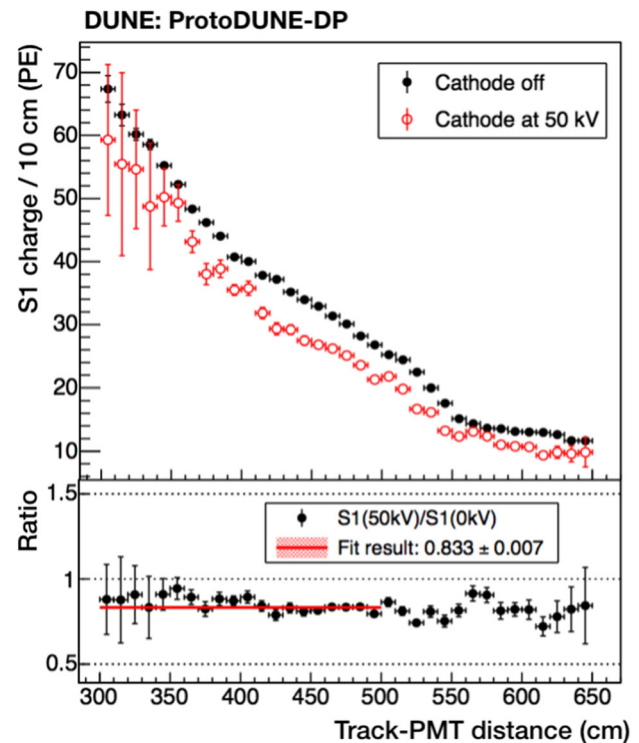


Fig. 17 Top panel: Average S1 charge collected by the PEN PMTs as a function of the track-PMT distance without drift field (black) and with cathode at −50 kV (red). The larger error bars at short distance are due to a lack of statistics. Bottom panel: Ratio between the two distributions. The ratio is fitted to a constant value (result: 0.833 ± 0.007)

pared to roughly quantify the light yield decrease. Figure 17 shows the charge-distance distributions at the two cathode HVs and the corresponding ratios between them. The ratio as a function of the track-PMT distance is fitted to a constant to obtain the average ratio of 0.833 ± 0.007 , which means that at least 17% of the scintillation light detected in the absence of a drift field comes from electron-ion recombination.

The CRT-trigger muons cross different fields, which leads to a difficult quantification of the overall drift field responsible for the light level reduction. An estimate of the effective electric field along the CRT-trigger muon tracks was made using the 3D simulation of the drift field in ProtoDUNE-DP corresponding to a cathode HV of −50 kV, see Fig. 3. The average field value obtained for these tracks is $0.09^{+0.10}_{-0.02}$ kV/cm, where the errors are determined asymmetrically, as the RMS of the values above and below the mean value separately. The reduction of the S1 signal for this drift field is plotted in Fig. 18 and follows the empirical Birks’ law. Despite the relatively large uncertainty of the ProtoDUNE-DP result, a fair agreement is found with the literature for both ground-level cosmic muons [35] and MeV-electrons [49,50].

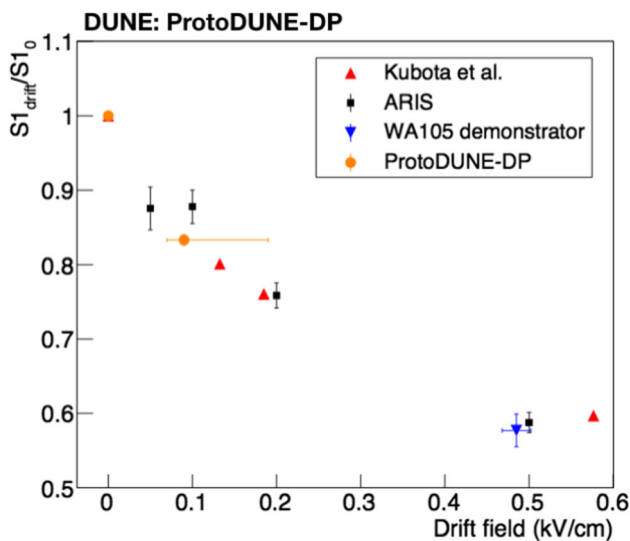


Fig. 18 Light yield reduction with drift field measured by various experiments (red triangles from [49], black squares from [50], blue inverted triangles from [35]), and the ProtoDUNE-DP result (orange circles) discussed in this section

The scintillation time profile is also dependent on the drift field. The two excited molecular states, singlet and triplet, are formed either through recombination or excitation with different probability, in such a way that the normalization constants, A_{fast} and A_{slow} of Eq. 6, are expected to change as a function of the drift field as the light emitted by electron-ion recombination is suppressed. According to [49] the ratio $(A_{fast} + A_{int})/A_{slow}$ is expected to decrease but the recent measurement presented in [35] shows an increase of 34% at 500 V/cm. ProtoDUNE-DP has observed an increase of 28% at -50 kV cathode voltage, corresponding to an average field value of $0.09^{+0.10}_{-0.02}$ kV/cm, which is consistent with the 23% measured in [35] at a similar electric field strength.

A decrease of τ_{slow} with the drift field was reported for the first time in [35] and is also observed in ProtoDUNE-DP, see Fig. 19. A model is proposed in [51], taking into account the quenching of the long-lived triplet states through the self-interaction with other triplet states or through the interaction with molecular Ar_2^+ ions. It successfully explains the experimentally observed dependence of τ_{slow} with the intensity of the applied electric field.

5.2 Light propagation

The size of ProtoDUNE-DP, the longest drift-distance LArTPC ever operated, allows for an unprecedented study of the light propagation. The Rayleigh scattering length (RSL) can impact on the amount of light collected. An evaluation of the RSL value is carried out by comparing the measured light signals with the light predicted by the MC simulation testing two lengths (61.0 cm [46] and 99.9 cm [45]) obtained

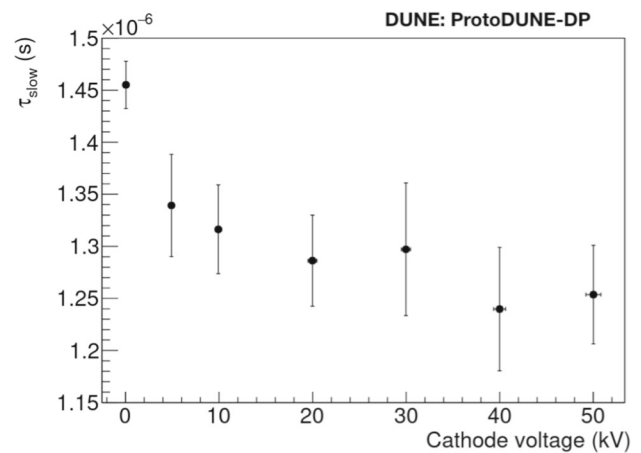


Fig. 19 Evolution of τ_{slow} with the cathode voltage for CRT-trigger events. The results are obtained averaging PEN PMTs and the error bars indicate the STD among them

in experimental measurements. Modeling the dependence of the light attenuation from the track-PMT distance with a decaying exponential function allows the measurement of the overall effective attenuation in data and MC and the evaluation of the agreement for the different simulated configurations. The track-PMT distance range studied is 4–5 m to focus on the longer distances where the sensitivity to the RSL effect is higher.

In Fig. 20, each S1 charge-distance correlation under study is fitted to an exponential and the data-MC ratios for the two simulations are also presented. Looking at the distribution shape, the agreement between data and the 99.9-cm MC sample is better than with the 61.0-cm value. The attenuation length values obtained are presented in Table 6, and it is observed that the data value also agrees better with the 99.9-cm MC value. The attenuation length accounts for the effective attenuation of the light in ProtoDUNE-DP, but it is not a physical property of the LAr as it depends, among other factors, on the topology of the selected tracks and detector geometry. The measured attenuation length is higher than the RSL, so the light is expected to undergo Rayleigh scattering before being heavily attenuated due to, for example, absorption by LAr impurities or detector elements. This long light path before absorption is achieved in ProtoDUNE-DP thanks to the excellent LAr purity and the large free LAr volume with no nearby components.

By comparing MC samples generated with the photon libraries (A) and (C), the impact of the VUV-photon reflections on the light reaching the PMT array can be evaluated. It is found that 11% of the light detected by PEN PMTs in the baseline MC corresponds to VUV light reflected on the field cage, cryostat walls, cathode and ground grid.

Finally, the light detection is studied through the effective TPB and PEN PMT efficiencies described in Sect. 3.3.

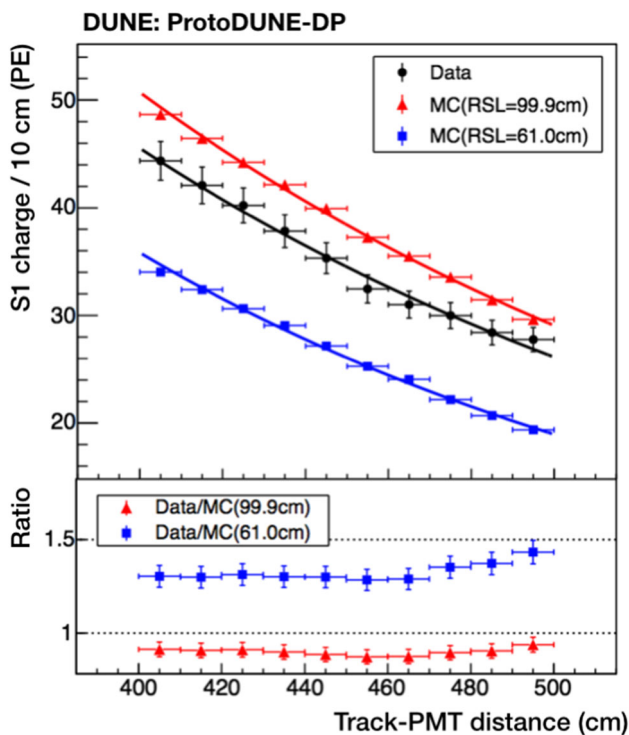


Fig. 20 Top panel: average S1 charge collected by the PEN PMTs as a function of the track-PMT distance. Two MC samples with different RSL values (61.0 cm and 99.9 cm) are compared to data. For each distribution, an exponential fit is plotted as a solid line. Bottom panel: data-MC ratio for the two previous MC samples

Table 6 Attenuation length values obtained from the exponential fits shown in Fig. 20

Sample	λ_{att} (cm)
Data	180 ± 17
MC (RSL 99.9 cm)	180 ± 10
MC (RSL 61.0 cm)	157 ± 8

The data-MC charge ratios obtained are 0.898 ± 0.002 and 1.150 ± 0.005 for PEN and TPB PMTs, respectively, in the selected track-PMT distance range. The result is that the simulation efficiency is validated within 10–15% of data. The simulation underestimates the light detected by the TPB PMTs, which may be because not all the reflected light is simulated, or the TPB WLS efficiency may be under-estimated. However, the light detected by PEN PMTs in data is lower than in the simulations, which can be attributed to a PEN WLS efficiency over-estimation.

6 Measurement of the cosmic muon rate and light yield

The rate of cosmic particles crossing the detector is high because ProtoDUNE-DP is located on the surface. The high

rate represents a perfect test bench to study the PDS capability for detecting muons and providing calorimetric information.

The S1 rate and charge from cosmic muons crossing ProtoDUNE-DP as well as the muon flux are evaluated in Sect. 6.1. In addition, the observed light yield from muons is investigated for two different WLS methods in Sect. 6.2.

In total, five data sets acquired over seven months with the random trigger are analyzed and compared with CORSIKA-based simulations. The cosmic-muon data sample allows the validation of the PDS simulation to demonstrate that the detector response is correctly modeled and understood. CRT-trigger data are also analyzed to evaluate the detected light yield for different muon samples.

6.1 Measurement of the cosmic muon flux

The results shown in this section are based on the analysis of S1 signals from light data acquired in random-trigger mode. These data comprise varied signals as the light reaching the PMTs can be generated at any location within LAr volume and be associated with very different track topologies and energies.

The muon S1 signals are identified in the PMT waveforms using a custom peak-finding algorithm which takes the following aspects into account:

1. Any pulse in the waveform with an amplitude larger than the expected SPE amplitude plus 2σ is considered a candidate S1 signal. The amplitude threshold is based on the results of the average SPE amplitude presented in Sect. 3.2. The lack of τ_{int} in the simulated scintillation time profile (see Sect. 4) results in a different charge-amplitude correlation than in data and, hence, a correction of the amplitude is applied in the MC analysis in order to select events that correspond to the same deposited energy as in data.
2. After a candidate S1 signal, a veto time window of $4.8 \mu s$ is applied. If another candidate S1 signal is detected during that time, a new $4.8\text{-}\mu s$ veto window beginning at that point is imposed.
3. An optical reconstruction to reject small and uncorrelated signals is performed by requiring coincidences among PMTs. A coincidence occurs when at least two PMTs detect the candidate S1 signal within a time interval of 112 ns. This cut is effective in rejecting candidate S1 signals at low energy in data, where the background, which is not considered in the MC, is dominant. About 40% and 10% of candidate S1 signals are rejected in data and MC, respectively.

The rate of S1 signals detected by each PMT is then computed. It should be noted that the obtained S1 rate is not the overall cosmic muon rate in the detector but the aver-

Table 7 Average S1 rate per PMT in random-trigger mode and data/MC ratio. The error of the S1 rate corresponds to the STD among PMTs

PMT	S1 rate per PMT (kHz)		Data/MC ratio
	Data	MC	
TPB	8.8 ± 0.5	10.2 ± 0.5	0.86 ± 0.09
PEN	5.5 ± 0.6	6.1 ± 0.4	0.90 ± 0.10

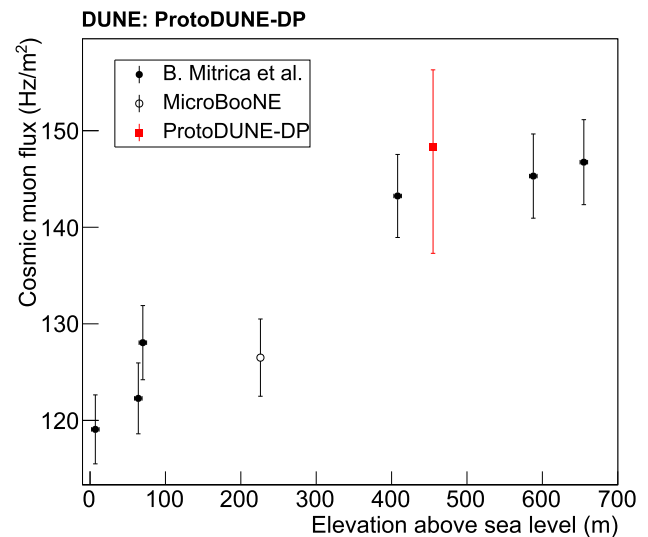
age muon rate per PMT. Results presented in Table 7 show a higher rate of simulated S1 signals induced by muons: around 16% (11%) higher S1 rates are detected by the TPB (PEN) PMTs in simulation than in data. Nevertheless, the muon flux with the model chosen within CORSIKA to generate the primary cosmic particles, the CMC model, is expected to be up to 20% above the one obtained with a model assuming only cosmic protons, as reported in [52], and the flux can be up to 25% lower with other particle generators. Thus, the observed data-MC deviation is within the discrepancy between the cosmic-ray generator models.

Finally, the atmospheric muon flux is assessed. Considering the surface covered by the PMT array and the fraction of muons crossing such an effective area in the MC, the predicted atmospheric muon flux at the Earth's surface by CORSIKA is 166 Hz/m^2 . Then, the predicted flux is scaled by the ratio between the data and MC rates given in Table 7. A cosmic muon flux of $148_{-11}^{+8} \text{ Hz/m}^2$ is obtained in ProtoDUNE-DP at CERN (at 455 m altitude above mean sea level). The systematic uncertainty on the flux is computed by varying the threshold in amplitude for the S1 identification by $\pm 20\%$ (~ 10 -25 ADC) given the uncertainty in the MC waveform simulation, and the PMT efficiency in the MC by $\pm 10\%$ as concluded in Sect. 5. The ProtoDUNE-DP cosmic muon flux result is found to be consistent with other measurements at ground-level given in the literature, as can be seen in Fig. 21.

6.2 Observed light yield from cosmic muons

The light yield for muon interactions observed by the PDS is investigated considering the use of the system as a calorimeter. The event selection of random-trigger data explained in Sect. 6.1 is applied. Good stability among data taken throughout seven months in terms of S1 rate and charge collection (2–5% of STD among different sets in both cases) is observed, which indicates stable performance of the system.

Taking into account all the cosmic muon tracks across the LAr volume, the average deposited energy per muon is determined with the CORSIKA cosmic-ray simulation to be 813 MeV. Then, the observed light yield in random trigger mode is calculated as the total S1 charge collected by all PMTs normalized by the average deposited energy per muon. The results can be seen in Table 8. This approach is validated by the fair agreement between the total S1 charge collected by

**Fig. 21** Cosmic muon flux determined in ProtoDUNE-DP at CERN at 455 m above mean sea level (red square) compared to the measurements reported in [52] (filled black dots) and [53] (open black dot)**Table 8** Total S1 charge per cosmic muon (sum of all PMTs detecting a S1 signal) and observed light yield (average value from events and maximum value reached in an event) for two trigger modes. All the values obtained from data

Trigger	PMTs	S1 charge per muon (PE)	Obs. light yield (PE/MeV)	
			Avg.	Max.
Random	All	1830	2.3	21.4
	6 TPB	650	0.8	10.2
	30 PEN	1180	1.5	13.1
CRT	All	1320	0.7	2.1
	6 TPB	590	0.3	1.1
	30 PEN	730	0.4	1.0

the PDS per muon in data (1830 PE) and MC (1990 PE), see Fig. 22. In a similar way, the observed light yield is computed for S1 signals acquired with the CRT trigger, see Table 8. In this case, based on the average track length in LAr observed in data (9.4 m), an average deposited energy per muon of 1880 MeV is obtained.

According to the values in Table 8, the complete PDS of ProtoDUNE-DP (36 PMTs) detects about 2.3 PE/MeV and 0.7 PE/MeV for random-trigger and CRT-trigger muon tracks, respectively. The latter case corresponds to an average track-PMT distance of 475 cm whereas the former comprises muons crossing the detector at all distances from the PMTs (from close to distant tracks, up to 7 m away from the PMTs). Since the scintillation photons from cosmic muons triggered with the CRTs are produced farther from the PMTs, the light is expected to undergo more attenuation. It is worth commenting that the difference between the average and maximum observed light yields is wider for random trigger

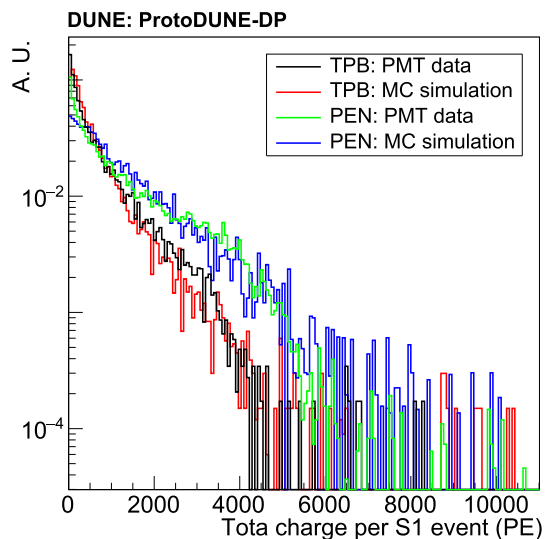


Fig. 22 Normalized distributions of the total S1 charge per cosmic muon event (sum of all detecting PMTs) in random trigger. Both data and MC (TPB and PEN) cases are displayed. The ADC saturation in data that limits the charge range is fairly reproduced in the MC

(almost 10 times) than for CRT-trigger events (3 times) due to the larger variety of events (energies and track topologies) in the first case.

The light yield is also shown in Table 8 separately for the two WLS groups in order to highlight the fact that the 6 TPB PMTs alone collect 1/3 of the total light. It can be concluded that if the 36 PMTs had TPB coating (PEN foil), a detection of about 5 PE/MeV (2 PE/MeV) would be reached in random trigger, on average. Therefore, in this particular PDS configuration, the use of PEN as the only WLS option would compromise the capability of the system as a calorimeter for low-energy particles. Considering TPB as the baseline WLS would make the low-energy physics goals of the DUNE Far Detector, such as triggering on a supernova neutrino burst, more feasible to accomplish.

In conclusion, the better detection efficiency of the TPB-coated PMTs together with their stable performance during the detector operation confirm that TPB is a better WLS choice for future LArTPCs. However, the mechanical advantages of PEN make it a good candidate if the emission efficiency is not critical.

7 Electroluminescence light detection

The electrons extracted into the gas phase produce produces a secondary scintillation signal, called S2, which is proportional to the drifted charge. The S2 signal provides information on the drifted electrons and the track topology. For instance, the time spread of the S2 signal is related to the track

topology, as the more inclined the track is, the larger the S2 time spread is. The time difference between the S2 signal and the S1 peak corresponds to the drift time that takes to the electrons produced by the ionizing particles to the anode.

In ProtoDUNE-DP, S2 electroluminescence signals are detected in all PMTs when extraction and amplification fields are on, corresponding to light originating about 7 m away from the PMTs. This detection is achieved thanks to the good LAr optical properties and purity and the high efficiency of the ProtoDUNE-DP PDS. In Fig. 23 an example event with S2 signal detected by all PMTs is shown. This is the first time light produced at such a large distance has been detected in a LArTPC.

ProtoDUNE-DP operated on the surface and observed a high S1 rate, see Sect. 6. The S2 signals are mostly observed as an increase in SPE rate which increases from hundreds of kHz, see Sect. 3.2, up to several MHz (~ 2.5 MHz for TPB PMTs and ~ 1.1 MHz for PEN PMTs) when there is S2 light production (DP operation mode). It is clear that the S2 signals are an important and continuous contribution to the low-energy background in the PMT waveform when the extraction field is on.

As a result, not every S2 signal can be associated to its previous S1. Only very energetic events produce S2 signals that can be distinguished from the SPE background and associated to their previous S1. A dedicated algorithm was developed to select these events where the S2 signal can be distinguished from the SPE background and evaluate them in relation to their previous S1 signal.

An individual PMT waveform of a very energetic event selected by the algorithm can be seen in Fig. 24. In this case, a fast S1 signal can be seen followed by a S2 signal with a duration of ~ 2 ms. Other S1 signals from cosmic muons are also visible. The S2 signals are observed to cause an overshoot in the waveforms as the amount of charge collected in the PMT anode exceeds the discharging rate of the combined PMT and readout circuit ($1/RC$ constant), effectively shifting the waveform baseline during the pulse. Waveforms are processed offline to correct for this effect, as described in [35]. In Fig. 24 the PMT waveform before and after the overshooting correction is shown.

Figure 25 shows the average waveform of the events passing the algorithm. These are very energetic events corresponding mainly to vertical showers where the track passed through the liquid-gas interface, and the S2 maximum is produced right after the S1. In these events the average S1 charge detected per PMT is >700 PE and the S2 charge >30 kPE. S2 signals last ~ 2 ms. As illustrated in Fig. 3, vertical muons will traverse a field of ~ 0.2 kV/cm along the first two meters for which an electron drift velocity of ~ 1 mm/ μ s is expected [36]. This implies an expected S2 duration of ~ 2 ms, which is consistent with the observed time.

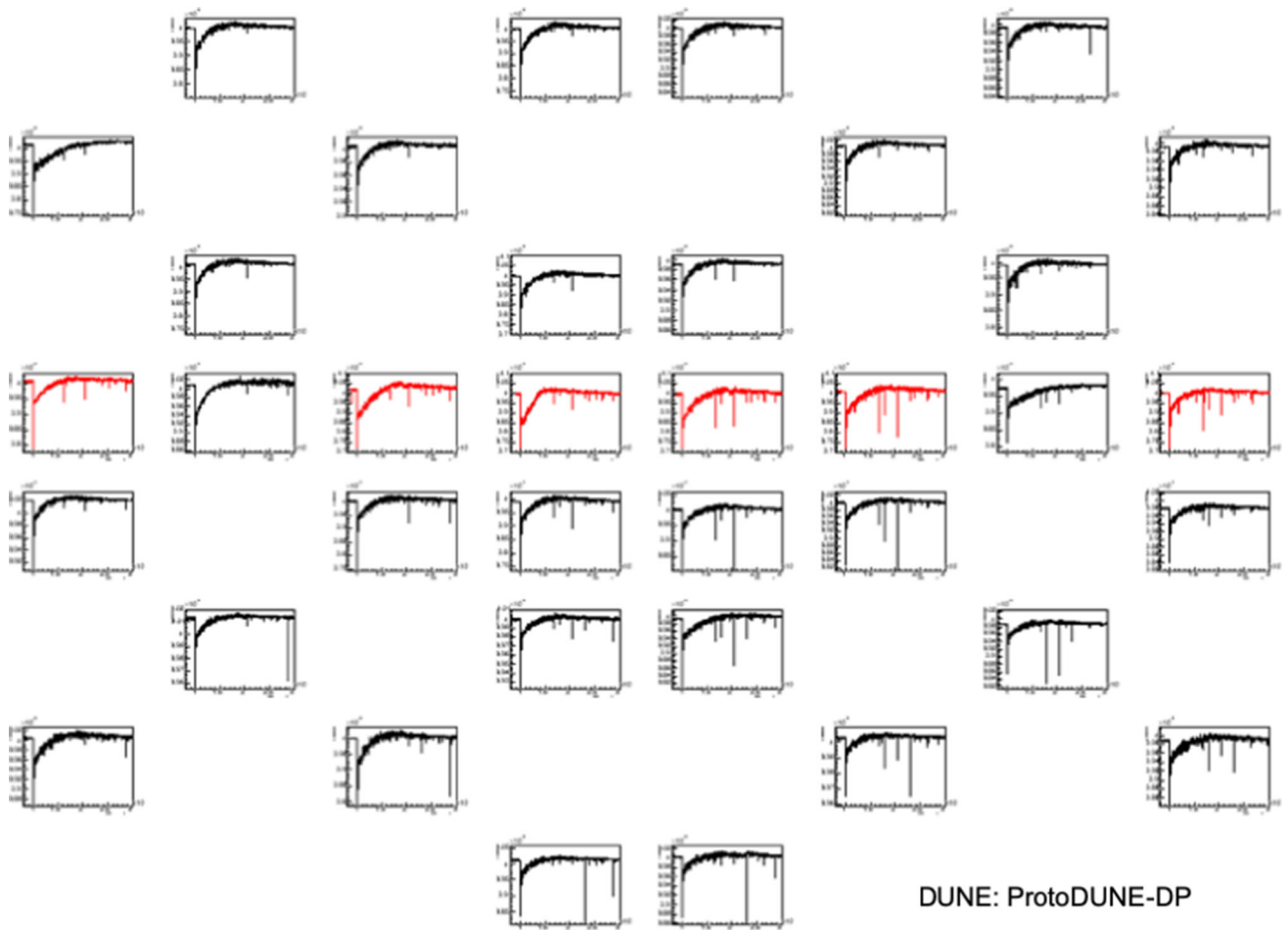


Fig. 23 Example of an event with S1 and S2 signals showing the waveforms corresponding to the 36 PMTs according to their relative position in the detector. PEN PMTs are shown in black and TPB PMTs in red.

The x -axis range is 0.8–3 ms for all PMTs while the y -axis range varies for each PMT and is optimized to best display the S2 signal

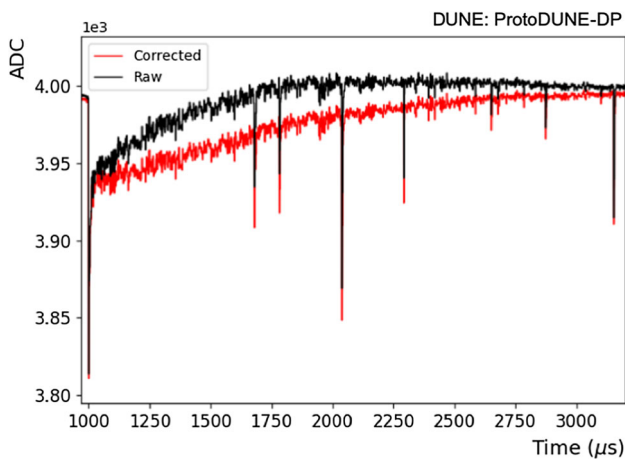


Fig. 24 Example of a scintillation light event in a ProtoDUNE-DP PMT at a gain of 10^7 in LAr with drift, amplification and extraction fields (S1 and S2 signal). The acquired waveform is shown in black and the resulting waveform after the overshooting correction in red

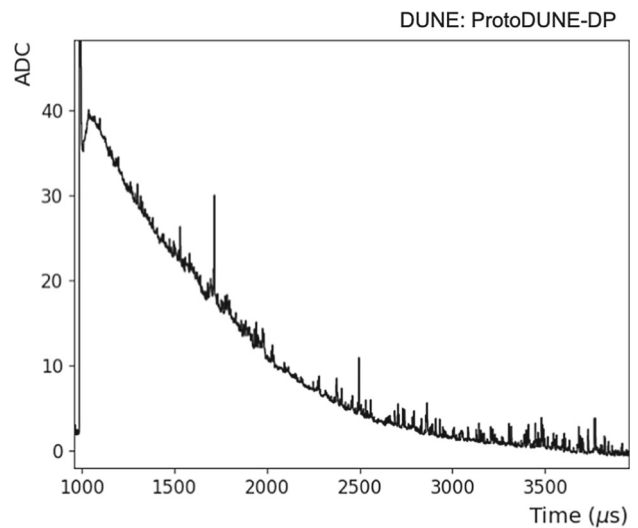


Fig. 25 Average waveform of PEN PMTs with a S2 signal identified. The y -axis is zoomed to focus on the S2 signal

8 Scintillation light in Xe-doped LAr

The use of Xe-doped LAr is a promising alternative to pure LAr for large-scale LArTPCs, since it mitigates the light suppression due to some impurities and it also improves the detection efficiency and uniformity.

In the presence of Xe, molecular Ar excimers in the triplet state live long enough to transfer their energy to the Xe atoms creating Xe excimers that decay and produce photons with a longer wavelength than 127 nm [54]. Therefore, the scintillation light is no longer monochromatic and has three components: Ar light at 127 nm, and Xe light at 178 nm and 150 nm, with significant contribution at 150 nm only at Xe concentrations below 1 ppm [55]. Since molecular Ar excimers in the singlet state decay too fast to transfer their energy, they produce 127-nm photons only, while the late light is dominated by 150-nm and 178-nm photons.

Xe doping also affects the photon propagation. On one hand, it is reported that Xe acts as an impurity, suppressing part of the spectrum at 127 nm even at the concentration of 0.1 ppm [56]. This absorption reduces the fast component of the detected signal. On the other hand, photons at longer wavelengths (150 and 178 nm) are not absorbed [56], and have a longer RSL. RSL is ~ 1 m for 127-nm photons while it is ~ 3.5 m for 150 nm and ~ 9 m for 178 nm photons [45]. A longer RSL enhances the light detection at longer distances with respect to pure LAr, since photons with a longer RSL scatter less and are able to travel further thereby improving the uniformity of detection.

The presence of nitrogen in LAr leads to the suppression of the light production due to a quenching process driven by two-body collisions of N_2 impurities with excited argon excimers [57]. This quenching affects mainly the excimers in the triplet state as the singlet state decays much faster. Since

quenching by N_2 and Xe excimer formation are competing processes, the Xe atoms mitigate the light suppression due to the N_2 .

Additionally, the absorption of photons by N_2 is expected to increase with the concentration, with a reported absorption length for 127-nm photons of 28 m at 1.7 ppm, 20 m at 2.7 ppm and 12 m at 4.7 ppm [44].

In the case of ProtoDUNE-DP, after the re-filling with ~ 230 ton of Xe-doped liquid argon contaminated with N_2 , as described in Sect. 2, both N_2 and Xe species were present in the LAr, altering the light production and propagation. The effect of the presence of Xe and N_2 in the detected light in ProtoDUNE-DP is studied using two types of muon-track signals: First, events triggered with a TPB-coated PMT placed at the center of the detector with a minimum amplitude of 25 PEs, for which the light is produced at a close distance from the PMTs, and second, CRT-trigger events, for which the PMT-track distance is in the range of 3–5 m.

Figure 26 shows the evolution of the total S1 charge detected by all PMTs as a function of time during the LAr evaporation from 7.4 to 5.1 m of liquid level, re-filling and N_2 injection steps. Around 12 kPEs are detected on average per PMT-trigger event, compared to only 2 kPEs per CRT-trigger event in LAr. The S1 signal is integrated over a long time window of 12 μ s after the maximum. The reduction of the collected light during the evaporation is visible for the CRT-trigger events, as part of the CRT-track is no longer in the liquid, while the collected light for the PMT-trigger tracks is stable. After the filling with Xe-doped LAr, the collected light increases as expected due to the longer RSL, and it decreases with the N_2 injections due to the quenching.

To quantify the impact of the presence of Xe and N_2 on the S1 charge and amplitude with respect to their values in pure LAr, data taken with the same liquid level are selected to

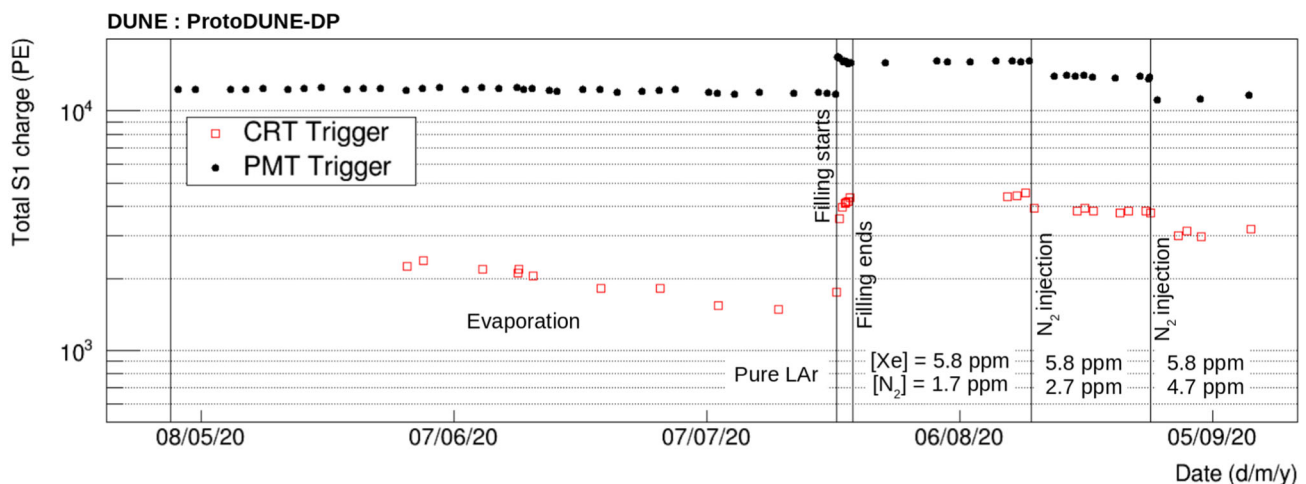


Fig. 26 Evolution of the average S1 charge per event detected in all the PMTs for PMT(CRT)-trigger data in black (red) during the evaporation, filling and N_2 injections. The processes are described in Sect. 2

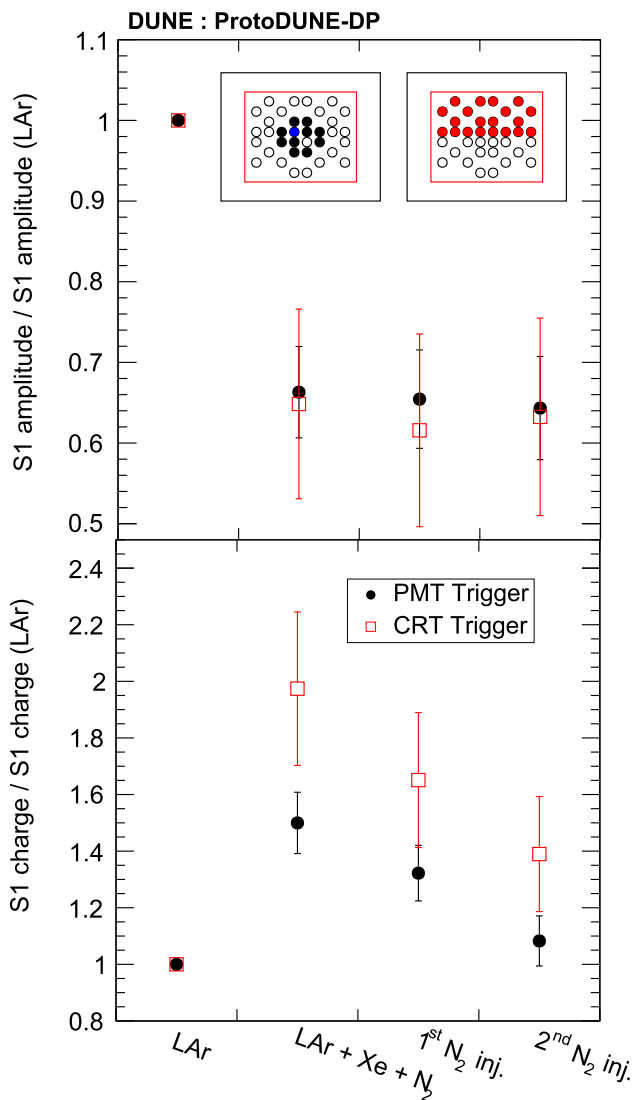


Fig. 27 Ratio of the average S1 amplitude and S1 charge in the three doping concentrations relative to pure LAr. PMT-trigger data are shown in black, and CRT-trigger in red. Only a selection of PMTs is considered for the average. Selected PMTs are marked as black (red) circles in the small diagram for the PMT(CRT)-trigger data. A blue circle marks the trigger PMT in the PMT-trigger diagram. Errors show the STD among the selected PMTs. Xe and N_2 concentrations for each situation are summarized in Table 1

ensure the same optical conditions. Figure 27 shows the average variation of the S1 amplitude and S1 charge for different detector conditions. Only PMTs placed near the trigger PMT are considered for PMT-trigger data analysis, to have a similar track-PMT distance, while only channels placed below the CRT-track are selected for CRT-trigger data analysis, since the other PMTs are placed more than five meters away from the track and for these distant PMTs the signal is dominated by background. The amplitude decreases 35% when adding 5.8 ppm of Xe and 2.4 ppm of N_2 with respect to pure LAr for both trigger modes, being unaffected by the N_2 addition. This

reduction is due to the absorption of the 127-nm photons by the Xe atoms as reported in [56]. Whilst a 16% decrease of the fast component (S1 amplitude) for the CRT-trigger data is expected when adding N_2 according to [44], we observe the fast component remaining constant for the two N_2 injections. A possible explanation for this discrepancy is that the assumption of the fast component being monochromatic at 127 nm is not accurate, and an additional light contribution at a different wavelength, that is not absorbed by the N_2 , is masking the expected absorption at 127 nm. The collected S1 charge increases 100% for the CRT-trigger data, while only 50% for the PMT-trigger data. This difference is understood as an improvement of the detection uniformity, since CRT-trigger muons are on average farther away from the PMTs, and the longer RSL of the Xe photons improves their collection at large distances. The decrease of the S1 charge due to the presence of N_2 is similar for both triggers (30%), meaning that there is no dependence of the detected light suppression on the PMT-track distance. This indicates that the reduction is mainly due to the quenching of the Ar excimers by N_2 rather than photo-absorption.

In order to evaluate the effect of the Xe-doping on the attenuation length (λ_{att}), a study of the dependence of the collected light per PMT with the track-PMT distance is performed for muon tracks crossing the CRT panels, see Fig. 28. The range of distances is given by the position of the PMTs with respect to the triggered track, which is always approximately in the same position (see Sect. 1). The behavior is not purely exponential since light absorption by the field cage introduces a border effect. A shoulder shape is observed at around 4.3 m, which corresponds to the PMTs placed at the center of the detector, where this effect is reduced. This limitation is due to the fixed geometry of the triggered tracks. An exponential fit is performed to estimate the attenuation length in each detector condition, and the results are summarized in Table 9. The effective attenuation length increases 60% when adding Xe, as expected because of the longer RSL, and decreases 5% when adding 2.9 ppm of N_2 . The lower panel of Fig. 28 shows the ratios of the top panel curves. The comparison between pure LAr and Xe-doped LAr in red shows the improved detection uniformity when adding Xe, with an increase of almost a factor of ~ 3 on events at 5 m

Table 9 Measured attenuation lengths in the different doping concentrations from the exponential fits shown in Fig. 28

Situation	[Xe](ppm)	[N_2](ppm)	λ_{att} (cm)
LAr	0	0	209 ± 5
LAr + Xe + N_2	5.8	2.4	338 ± 13
1 st N_2 inj.	5.8	3.4	332 ± 13
2 nd N_2 inj.	5.8	5.3	321 ± 12

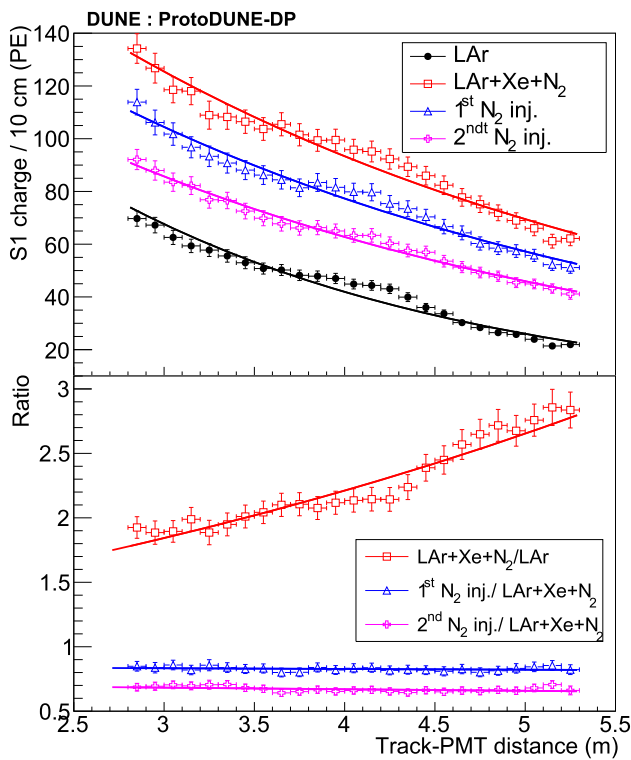


Fig. 28 Top panel: average collected S1 charge per PMT as a function of the track-PMT distance for the different doping concentrations. For each data-set, an exponential fit is performed (see results in Table 9). Bottom panel: ratios between the data shown in the top panel. Each data-set is fitted with an exponential function

and a factor of ~ 2 on events at 3 m. The extrapolation of this curve to short distances indicates an increase by a factor of 1.5 at 2.2 m, as seen in Fig. 27 for the PMT-trigger muons, and no increase at 0 m, as expected due to the longer RSL. The flat blue and magenta lines show that there is no dependence on the distance for the N_2 injections, as seen also in Fig. 27.

The effect of xenon on the time profile of the waveforms is also studied. Figure 29 shows the average waveforms for a TPB-coated PMT in the different doping concentrations described in Sect. 2 (pure LAr in black), normalized to the same amplitude. The average waveform is the result of adding waveforms for a PMT placed near the trigger PMT. The second bump in the red, blue and magenta waveforms (when Xe is present) is the late light at 150 nm and 178 nm, as explained before. The profile of this second maximum changes with the N_2 injections, as the energy transfer rate from argon to xenon atoms is altered due to the quenching by N_2 . The average waveforms of Xe-doped LAr are fitted to the sum of three exponential functions convolved with a Gaussian to account for the PMT response, in a similar way as in Eq. (6). In this case, the first exponential describes the fast signal, and the second and third exponential functions model the rise

Table 10 Time constants obtained from the fit of the average waveforms at the different doping concentrations. Errors show the variation among PMTs

Situation	$\tau_{transfer} (\pm 0.01\mu s)$	$\tau_{slow} (\pm 0.01\mu s)$
LAr	N/A	1.43
LAr + Xe + N_2	0.46	1.10
1 st N_2 injection	0.41	1.03
2 nd N_2 injection	0.35	0.91

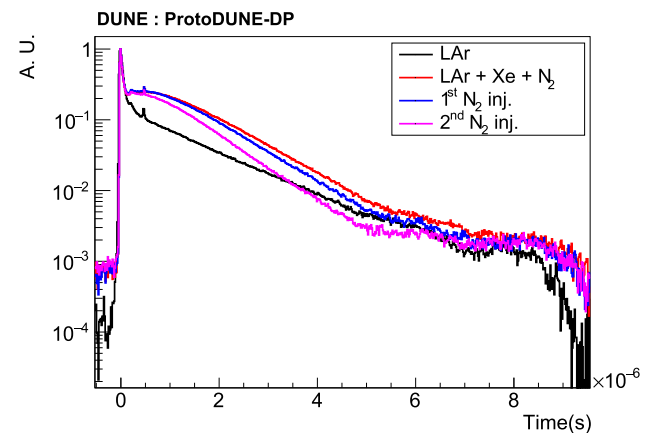


Fig. 29 PMT average waveform normalized to same amplitude in LAr (black), LAr + Xe + N_2 (red), after the 1st N_2 injection (blue) and after the 2nd N_2 injection (magenta). Concentrations are described in Table 9

($\tau_{transfer}$) and decay (τ_{slow}) of the second bump from the Xe light.

The time constants obtained from the fits are shown in Table 10. No difference between PEN-foil and TPB-coated PMTs is found.

In summary, ProtoDUNE-DP data show that Xe doping is a promising technique for large-scale detectors like DUNE since it increases the collected light at large distances. With a small doping level of 5.8 ppm of Xe (and even with the presence of 2.4 ppm of N_2), an enhancement in the light detection efficiency (100% increase for muons crossing at a distance of 3–5 m from the PMTs) and a better uniformity (attenuation length 50% longer) is measured. However, despite these advantages, it must be considered that the 35% amplitude reduction observed in the fast signal could jeopardize the efficiency of a light-based trigger.

9 Conclusions

ProtoDUNE-DP is a $6 \times 6 \times 6 \text{ m}^3$ LArTPC, operated at CERN between 2019 and 2020 to demonstrate the dual-phase technology at large scale for DUNE, a next generation long-baseline neutrino experiment. The photon detection system is composed of 36 8-inch cryogenic PMTs from Hamamatsu

positioned at the bottom of the detector. The photon detection system collected cosmic-ray data for 18 months in stable conditions with all 36 PMTs in operation. The good performance validates the photon detection system design for future long drift distance LArTPCs.

ProtoDUNE-DP used PEN as a wavelength shifter for the first time in a large scale experiment and a comparison with the widely used TPB is carried out. TPB is estimated to be 3 times more efficient than PEN. The observed light yield from cosmic muons demonstrates that a system based exclusively on TPB as WLS would be needed to accomplish the DUNE low-energy physics program goals. Nonetheless, PEN can be taken into account as an alternative when the detection efficiency is not critical compared to the benefits of easy installation.

In ProtoDUNE-DP, considering the field limitations, it is found that at least 17% of the scintillation light detected in the absence of a drift field comes from electron-ion recombination, verifying the expected trend from Birks' law and in agreement with previous work. A decrease of τ_{slow} with the drift field as reported in [35] is also observed. An explanation of this effect is provided in [51] taking into account the quenching of the long lived triplet states through the self-interaction with other triplet states or through the interactions with molecular argon ions.

The size of ProtoDUNE-DP allows for an unprecedented study of the light propagation. An evaluation of the Rayleigh scattering length is carried out by comparing the measured light signals with the light predicted by the MC simulation testing two lengths (61.0 cm and 99.9 cm). The agreement between data and the 99.9-cm MC sample is better than for the shorter scattering length. It is also concluded that at least 11% of the light detected by PMTs in the MC corresponds to VUV-light reflected off the field cage, cryostat walls, cathode and ground grid.

The cosmic muon flux in ProtoDUNE-DP at ground level is determined from the S1 signal rate detected by the PMTs and a cosmic-muon light simulation sample. The result, $148_{-11}^{+8} \text{ Hz/m}^2$, is consistent with other muon flux measurements in the literature [52, 53].

The electroluminescence light, S2, produced in the gas phase about 7 m away from the PMTs is observed in all 36 PMTs implying a high efficiency for the ProtoDUNE-DP photon detection system. The detected SPE rate increases up to several MHz when there is S2 light production, clear evidence that the S2 signals are an important and continuous contribution to the low-energy background in the PMT waveform.

Finally, ProtoDUNE-DP data has demonstrated the improvement of the light detection efficiency and uniformity in large LArTPCs, thanks to the Xe doping. A low doping level of 5.8 ppm of Xe doubles the collected light at large distances (3–5 m from the PMTs) even with the presence of 2.4 ppm

of N_2 . However, it must be considered that the reduction observed in the fast signal amplitude could compromise the performance of a light-based trigger.

Acknowledgements The ProtoDUNE-DP detector was constructed and operated on the CERN Neutrino Platform. We gratefully acknowledge the support of the CERN management, and the CERN EP, BE, TE, EN and IT Departments for NP04/ProtoDUNE-SP. This document was prepared by the DUNE collaboration using the resources of the Fermi National Accelerator Laboratory (Fermilab), a U.S. Department of Energy, Office of Science, HEP User Facility. Fermilab is managed by Fermi Research Alliance, LLC (FRA), acting under Contract No. DE-AC02-07CH11359. This work was supported by CNPq, FAPERJ, FAPEG and FAPESP, Brazil; CFI, IPP and NSERC, Canada; CERN; MŠMT, Czech Republic; ERDF, H2020-EU and MSCA, European Union; CNRS/IN2P3 and CEA, France; INFN, Italy; FCT, Portugal; NRF, South Korea; CAM, Fundación “La Caixa”, Junta de Andalucía-FEDER, MICINN, and Xunta de Galicia, Spain; SERI and SNSF, Switzerland; TÜBİTAK, Turkey; The Royal Society and UKRI/STFC, United Kingdom; DOE and NSF, United States of America. This research used resources of the National Energy Research Scientific Computing Center (NERSC), a U.S. Department of Energy Office of Science User Facility operated under Contract No. DE-AC02-05CH11231.

Data Availability Statement This manuscript has no associated data or the data will not be deposited. [Authors' comment: Data are stored at CERN and Fermilab servers and could be provided upon request.]

Open Access This article is licensed under a Creative Commons Attribution 4.0 International License, which permits use, sharing, adaptation, distribution and reproduction in any medium or format, as long as you give appropriate credit to the original author(s) and the source, provide a link to the Creative Commons licence, and indicate if changes were made. The images or other third party material in this article are included in the article's Creative Commons licence, unless indicated otherwise in a credit line to the material. If material is not included in the article's Creative Commons licence and your intended use is not permitted by statutory regulation or exceeds the permitted use, you will need to obtain permission directly from the copyright holder. To view a copy of this licence, visit <http://creativecommons.org/licenses/by/4.0/>.

Funded by SCOAP³. SCOAP³ supports the goals of the International Year of Basic Sciences for Sustainable Development.

References

1. B. Abi et al., JINST **15**(08), T08008 (2020). <https://doi.org/10.1088/1748-0221/15/08/T08008>
2. B. Abi et al., Eur. Phys. J. C **80**(10), 978 (2020). <https://doi.org/10.1140/epjc/s10052-020-08456-z>
3. B. Abi et al., Eur. Phys. J. C **81**(4), 322 (2021). <https://doi.org/10.1140/epjc/s10052-021-09007-w>
4. B. Abi et al., Eur. Phys. J. C **81**(5), 423 (2021)
5. B. Abi et al., JINST **15**(08), T08010 (2020). <https://doi.org/10.1088/1748-0221/15/08/T08010>
6. B. Abi, et al., *The DUNE Far Detector Interim Design Report, Volume 3: Dual-Phase Module* (2018). [arXiv:1807.10340](https://arxiv.org/abs/1807.10340)
7. L. Agostino, et al. LBNO-DEMO: Large-scale neutrino detector demonstrators for phased performance assessment in view of a long-baseline oscillation experiment, CERN-SPSC-2014-013, SPSC-TDR-004 (2014). [arXiv:1409.4405](https://arxiv.org/abs/1409.4405)

8. C. Cuesta, in *2019 European Physical Society Conference on High Energy Physics* (2019). [arXiv:1910.10115](https://arxiv.org/abs/1910.10115)
9. B. Aimard et al., *J. Instrum.* **16**(08), P08063 (2021). <https://doi.org/10.1088/1748-0221/16/08/p08063>
10. A. Chappuis, Study and simulation of the scintillation light produced and propagating in a dual phase liquid argon time projection chamber, in the context of the DUNE experiment. Theses, Université Grenoble Alpes (2018). <https://tel.archives-ouvertes.fr/tel-02146587>
11. T. Heindl et al., *EPL* **91**(6), 62002 (2010). <https://doi.org/10.1209/0295-5075/91/62002>
12. A. Hitachi et al., *Phys. Rev. B* **27**, 5279 (1983). <https://doi.org/10.1103/PhysRevB.27.5279>
13. C. Cuesta et al., *JINST* **12**, C12048 (2017). <https://doi.org/10.1088/1748-0221/12/12/C12048>
14. D. Belver et al., *JINST* **13**, T10006 (2018). (8/1748-0221/13/10/T10006)
15. D. Belver et al., *JINST* **15**(09), P09023 (2020). <https://doi.org/10.1088/1748-0221/15/09/P09023>
16. D. Belver et al., *JINST* **14**(04), T04001 (2019). <https://doi.org/10.1088/1748-0221/14/04/T04001>
17. J.S. Kapustinsky et al., *NIMA* **241**, 612 (1985). [https://doi.org/10.1016/0168-9002\(85\)90622-9](https://doi.org/10.1016/0168-9002(85)90622-9)
18. Comsol multiphysics® v. 5.4. www.comsol.com
19. B. Abi et al., *JINST* **15**(12), P12004 (2020). <https://doi.org/10.1088/1748-0221/15/12/P12004>
20. D. Belver et al., *IEEE Trans. Nucl. Sci.* **68**(9), 2334 (2021). <https://doi.org/10.1109/TNS.2021.3095355>
21. V1740-64 channel 12 bit 62.5 ms/s digitizer-caen. <https://www.caen.it/products/v1740/>. Accessed 05 Oct 2021
22. P. Benetti et al., *Nucl. Instrum. Methods A* **574**, 83 (2007). <https://doi.org/10.1016/j.nima.2007.01.106>
23. A.S. Barabash, R.R. Saakyan, V.I. Umatov, *J. Phys. Conf. Ser.* **718**(6), 062004 (2016). <https://doi.org/10.1088/1742-6596/718/6/062004>
24. X. Luo, F. Cavanna, *JINST* **15**(03), C03034 (2020). <https://doi.org/10.1088/1748-0221/15/03/C03034>
25. M. Bonesini, T. Cervi, A. Falcone, U. Kose, R. Mazza, A. Menegolli, C. Montanari, M. Nessi, M. Prata, A. Rappoldi, G. Raselli, M. Rossella, M. Spanu, M. Torti, W. Vollenberg, A. Zani, *J. Instrum.* **13**(12), P12020 (2018). <https://doi.org/10.1088/1748-0221/13/12/p12020>
26. Polyethylene naphthalate (pen)-film-material information. <http://www.goodfellow.com/E/Polyethylene-naphthalate-Film.html>. Accessed 05 Oct 2021
27. D. Mary et al., *J. Phys. D Appl. Phys.* **30**, 171 (1997). <https://doi.org/10.1088/0022-3727/30/2/004>
28. R. Francini et al., *JINST* **8**(09), P09006 (2013). <https://doi.org/10.1088/1748-0221/8/09/p09006>
29. Y. Abraham, et al. Wavelength-shifting performance of polyethylene naphthalate films in a liquid argon environment (2021). [arXiv:2103.03232](https://arxiv.org/abs/2103.03232)
30. A. Bueno, J. Lozano, A.J. Melgarejo, F.J. Muñoz, J.L. Navarro, S. Navas, A.G. Ruiz, *J. Instrum.* **3**(01), P01006 (2008). <https://doi.org/10.1088/1748-0221/3/01/p01006>
31. Q. Zhao, M. Guan, P. Zhang, C. Yang, J. Li, Y. Wei, L. Wang, Y. Gan, W. Xiong, *J. Instrum.* **16**(06), T06014 (2021). <https://doi.org/10.1088/1748-0221/16/06/t06014>
32. C. Benson et al., *Eur. Phys. J. C* **78**, 329 (2018). <https://doi.org/10.1140/epjc/s10052-018-5807-z>
33. J.R. Graybill, C.B. Shahi, M.A. Coplan, A.K. Thompson, R.E. Vest, C.W. Clark, *Appl. Opt.* **59**(4), 1217 (2020). <http://ao.osa.org/abstract.cfm?URI=ao-59-4-1217>
34. C.H. Lally, G.J. Davies, W.G. Jones, N.J.T. Smith (1995)
35. B. Aimard et al., *JINST* **16**(03), P03007 (2021). <https://doi.org/10.1088/1748-0221/16/03/P03007>
36. C.F. Lastoria, Analysis of the scintillation light production and propagation in the WA105 Dual-Phase demonstrator. Análisis de la producción y propagación de la luz de centelleo en el detector de doble-fase WA105 (2020). <http://cds.cern.ch/record/2748990>. Presented 17 Dec 2020
37. E. Segreto, *Phys. Rev. C* **91**(3), 035503 (2015). <https://doi.org/10.1103/PhysRevC.91.035503>
38. D. Whittington et al., *JINST* **11**(05), P05016 (2016). <https://doi.org/10.1088/1748-0221/11/05/P05016>
39. E.L. Snider, G. Petrillo, *J. Phys. Conf. Ser.* **898**(4), 042057 (2017). <https://doi.org/10.1088/1742-6596/898/4/042057>
40. S. Agostinelli et al., *Nucl. Instrum. Methods A* **506**, 250 (2003). [https://doi.org/10.1016/S0168-9002\(03\)01368-8](https://doi.org/10.1016/S0168-9002(03)01368-8)
41. D. Heck, J. Knapp, J.N. Capdevielle, G. Schatz, T. Thouw (1998)
42. C. Forti, H. Bilokon, B. d'Ettorre Piazzoli, T.K. Gaisser, L. Satta, T. Stanev, *Phys. Rev. D* **42**, 3668 (1990). <https://doi.org/10.1103/PhysRevD.42.3668>
43. T.T. Böhlen, F. Cerutti, M.P.W. Chin, A. Fassò, A. Ferrari, P.G. Ortega, A. Mairani, P.R. Sala, G. Smirnov, V. Vlachoudis, *Nucl. Data Sheets* **120**, 211 (2014). <https://doi.org/10.1016/j.nds.2014.07.049>
44. B.J.P. Jones, C.S. Chiu, J.M. Conrad, C.M. Ignarra, T. Katori, M. Toups, *JINST* **8**, P07011 (2013). <https://doi.org/10.1088/1748-0221/8/07/P07011> (Erratum: *JINST* **8**, E09001 (2013))
45. M. Babicz et al., *JINST* **15**(09), P09009 (2020). <https://doi.org/10.1088/1748-0221/15/09/P09009>
46. E. Grace, A. Butcher, J. Monroe, J.A. Nikkel, *Nucl. Instrum. Methods Phys. Res. Sect. A Accel. Spectrom. Detect. Assoc. Equip.* **867**, 204 (2017). <https://doi.org/10.1016/j.nima.2017.06.031>
47. M. Antonello, et al., Technical Report ICARUS-TM/06-03 (2006)
48. B. Zatschler, Attenuation of the scintillation light in liquid argon and investigation of the double beta decay of ^{76}Ge into excited states of ^{76}Se in the GERDA experiment. Ph.D. thesis, Dresden, Tech. U., TU, Dresden (main) (2020)
49. S. Kubota et al., *Phys. Rev. B* **20**, 3486 (1979). <https://doi.org/10.1103/PhysRevB.20.3486>
50. P. Agnes et al., *Phys. Rev. D* **97**(11), 112005 (2018). <https://doi.org/10.1103/PhysRevD.97.112005>
51. E. Segreto, *Phys. Rev. D* **103**(4), 043001 (2021). <https://doi.org/10.1103/PhysRevD.103.043001>
52. P. Abratenko et al., *J. Instrum.* **16**(04), P04004 (2021). <https://doi.org/10.1088/1748-0221/16/04/p04004>
53. B. Mitrica, R. Margineanu, S. Stoica, M. Petcu, I. Brancus, A. Jipa, I. Lazanu, O. Sima, A. Haungs, H. Rebel, M. Petre, G. Toma, A. Saftoiu, D. Stanca, A. Apostu, C. Gomoiu, *Nucl. Instrum. Methods Phys. Res. Sect. A Accel. Spectrom. Detect. Assoc. Equip.* **654**(1), 176 (2011)
54. S. Kubota, M. Hishida, S. Himi, J. Suzuki, J. Ruan, *Nucl. Instrum. Methods Phys. Res. Sect. A Accel. Spectrom. Detect. Assoc. Equip.* **327**(1), 71 (1993)
55. A. Neumeier, T. Dandl, T. Heindl, A. Himpsl, L. Oberauer, W. Potzel, S. Roth, S. Schönert, J. Wieser, A. Ulrich, *EPL (Europhysics Letters)* **109**(1), 12001 (2015). <https://doi.org/10.1209/0295-5075/109/12001>
56. A. Neumeier, T. Dandl, A. Himpsl, L. Oberauer, W. Potzel, S. Schönert, A. Ulrich, *EPL (Europhysics Letters)* **111**(1), 12001 (2015). <https://doi.org/10.1209/0295-5075/111/12001>
57. R. Acciarri et al., *Nuc. Phys. B Proc. Suppl.* **197**, 70 (2009). <https://doi.org/10.1016/j.nuclphysbps.2009.10.037>